bioRxiv preprint doi: https://doi.org/10.1101/2024.02.02.578510; this version posted February 7, 2024. The copyright holder for this preprint (which was not certified by peer review) is the author/funder, who has granted bioRxiv a license to display the preprint in perpetuity. It is made available under aCC-BY-NC-ND 4.0 International license.

Gene regulatory network topology governs resistance and treatment escape in glioma stem-like cells

James H. Park[1], Parvinder Hothi[2], Adrian Lopez Garcia de Lomana[3], Min Pan[1], Rachel Calder[1], Serdar Turkarslan[1], Wei-Ju Wu[1], Hwahyung Lee[2], Anoop P. Patel[4,5], Charles Cobbs[2], Sui Huang[1], Nitin S. Baliga[1,6,*]

1. Institute for Systems Biology, Seattle, WA.
2. Ivy Center for Advanced Brain Tumor Treatment, Swedish Neuroscience Institute, Seattle, WA.
3. Center for Systems Biology, University of Iceland, Reykjavik, Iceland.
4. Department of Neurosurgery, Preston Robert Tisch Brain Tumor Center, Duke University, Durham, NC.
5. Center for Advanced Genomic Technologies, Duke University, Durham, NC
6. Departments of Microbiology, Biology, and Molecular Engineering Sciences, University of Washington, Seattle, WA.

Corresponding author email: nitin.baliga@isbscience.org

Teaser:

Gene regulatory networks drive glioma stem-like cell drug response and drug-induced cell-state transitions leading to resistance.

bioRxiv preprint doi: https://doi.org/10.1101/2024.02.02.578510; this version posted February 7, 2024. The copyright holder for this preprint (which was not certified by peer review) is the author/funder, who has granted bioRxiv a license to display the preprint in perpetuity. It is made available under aCC-BY-NC-ND 4.0 International license.

ABSTRACT

Poor prognosis and drug resistance in glioblastoma (GBM) can result from cellular heterogeneity and treatment-induced shifts in phenotypic states of tumor cells, including dedifferentiation into glioma stem-like cells (GSCs). This rare tumorigenic cell subpopulation resists temozolomide, undergoes proneural-to-mesenchymal transition (PMT) to evade therapy, and drives recurrence. Through inference of transcriptional regulatory networks (TRNs) of patient-derived GSCs (PD-GSCs) at single-cell resolution, we demonstrate how the topology of transcription factor interaction networks drives distinct trajectories of cell state transitions in PD-GSCs resistant or susceptible to cytotoxic drug treatment. By experimentally testing predictions based on TRN simulations, we show that drug treatment drives surviving PD-GSCs along a trajectory of intermediate states, exposing vulnerability to potentiated killing by siRNA or a second drug targeting treatment-induced transcriptional programs governing non-genetic cell plasticity. Our findings demonstrate an approach to uncover TRN topology and use it to rationally predict combinatorial treatments that disrupts acquired resistance in GBM.

bioRxiv preprint doi: https://doi.org/10.1101/2024.02.02.578510; this version posted February 7, 2024. The copyright holder for this preprint (which was not certified by peer review) is the author/funder, who has granted bioRxiv a license to display the preprint in perpetuity. It is made available under aCC-BY-NC-ND 4.0 International license.

INTRODUCTION

Glioblastoma (GBM) is the most lethal and aggressive primary brain tumor in adults. With current standard of care (SOC), which involves maximal surgical resection, fractionated radiotherapy (XRT), and chemotherapy with the DNA-alkylating agent, temozolomide (TMZ) (*1*), patient prognosis remains dismal with a median survival time of 14-15 months and a 90% risk of recurrence. There is growing evidence that the poor therapy responsiveness and dismal prognosis in GBM patients emerges from the interplay of tumor cell heterogeneity and treatment-induced shifts of cellular phenotypic states. Three molecular subtypes of GBM have been identified – proneural (PN), classical (CL), and mesenchymal (MES), each exhibiting distinct responses to SOC and clinical prognosis (*2*, *3*). Single-cell resolution transcriptome analyses further demonstrated that even an individual GBM tumor consist of highly heterogeneous cell populations, not only morphologically but also with respect to its composition of cellular states (*4*), which can include a mixture of PN/CL/MES subtype cells and a small subpopulation of glioma stem-like cells (GSCs) that have the capability to self-renew, generate different tumor cell progenies, and initiate new tumors. Further, there is evidence that extrinsic signals and stressors, including those generated by treatment, can also drive heterogeneous tumor cells to dedifferentiate into immature GSCs that are inherently resistant to TMZ (*5*, *6*).

While PN GSCs have higher proliferation rates and promote tumor angiogenesis, MES GSCs have potent invasive capabilities (*7*) and are more resistant to radiation (*8*) and drug treatment (*9*). Thus, most recurrent tumors derived from non-MES primary tumor are comprised of the MES subtype (*10*, *11*). Two hypotheses have been proposed for the shift in recurrent tumor subtype and corresponding development of treatment resistance (*12*, *13*): 1) MES subtype GSCs pre-existing in the heterogeneous tumor cell population are selected for and eventually drive the growth of the recurrent tumor (*14*); 2) radiation and chemotherapy causes GSCs to undergo a cell state conversion, namely a PN to MES transition (PMT) to evade and survive treatment (*7*, *15*). The latter hypothesis is in line with the emerging notion that non-genetic cell plasticity, in addition to selection of fixed, genetically determined phenotypes of mutant cells accounts for tumor progression and recurrence. For instance, radiation- or chemotherapy-induced epithelial to MES transition (EMT) in solid tumors has been widely implicated in the rapid development of therapy resistance (*16*–*25*). Thus, GSCs undergoing PMT may be causally responsible for recurrence of most drug resistant GBM tumors in the form of the MES subtype (*26*). For example, expression of MES marker (CD44) and NF-kB pathways associated with PMT were elevated following

bioRxiv preprint doi: https://doi.org/10.1101/2024.02.02.578510; this version posted February 7, 2024. The copyright holder for this preprint (which was not certified by peer review) is the author/funder, who has granted bioRxiv a license to display the preprint in perpetuity. It is made available under aCC-BY-NC-ND 4.0 International license.

radiation treatment of PN GSCs pre-treated with TNF-α. In genetically engineered mouse models with cells that can fluorescently report molecular subtype, GSCs transitioned to the MES subtype as early as 6 hours following radiation treatment, demonstrating intrinsic ability of GSCs to deal with treatment-induced stress (*15*). Finally, GSCs isolated from the invasive tumor edge transitioned from a PN subtype to a MES phenotype in a C/EBP-β dependent manner following treatment (*27*). In view of the accumulating evidence for the role of non-genetic plasticity of GSCs in the development of recurrent and refractory tumors, understanding the mechanisms underlying GSC plasticity is critical to address its role in disease progression and the unintended consequences of treatment. Although multiple clinical trials are underway to evaluate novel drugs or drug combinations that are both cytotoxic against GSCs and also meet the criteria for treating brain tumors (e.g., penetrance of blood brain barrier) and recurrent therapy-refractory GBM (*28*), these clinical studies, including our own, have discovered that many FDA-approved drugs are effective in killing GSCs, but can also induce surviving cells to undergo PMT.

Here, we sought to understand if knowledge of mechanisms underlying the developmental plasticity of GSCs, and the trajectories through which these cells undergo drug-induced PMT, would enable rational strategies to improve treatment responsiveness by disrupting primary resistance mechanisms, by blocking therapy escape to prevent acquired resistance and tumor recurrence. We have performed these studies with pitavastatin, an HMG-CoA reductase inhibitor, which is widely used to manage cholesterol levels. Pitavastatin is a prime example of an FDA-approved drug that can be repurposed to minimize GBM recurrence because of its anti-proliferative and radiotherapy sensitization effects on glioma cells (*29*), its cytotoxic effects against GSCs (*30*), and because of its recent evaluation for use in combination therapy (*31*). Specifically, we have investigated mechanisms of primary and acquired resistance in six patient-derived GSCs (PD-GSCs) – three responders (SN520, SN533, and SN575) and three non-responders (SN503, SN517 and SN521) to pitavastatin. Through the inference of mechanistic transcriptional regulatory networks at single-cell resolution, we demonstrate that the architecture and dynamics of a core transcription factor (TF) network governed the phenotypic plasticity of PD-GSCs. By performing *in silico* simulations and chemical and genetic (siRNA) perturbations, we show compelling evidence that it wasn't the composition of initial cell states, but the topology of the core TF-TF network that governed phenotypic plasticity of GSCs. Finally, our findings demonstrate that mechanistic knowledge of the gene regulatory network topology can be leveraged to rationally tailor combinatorial and sequential treatment regimen to disrupt primary or acquired resistance in a given PD-GSC.

bioRxiv preprint doi: https://doi.org/10.1101/2024.02.02.578510; this version posted February 7, 2024. The copyright holder for this preprint (which was not certified by peer review) is the author/funder, who has granted bioRxiv a license to display the preprint in perpetuity. It is made available under aCC-BY-NC-ND 4.0 International license.

RESULTS

Pitavastatin treatment induces distinct responses in SN520 and SN503 PD-GSCs

Through high throughput dose titration assays, we discovered that pitavastatin had a wide range of effectiveness against 45 PD-GSCs. Based on their varying sensitivities, we classified the PD-GSCs into two categories, one in which PD-GSCs were considered a “responder” (IC50 < 5.0μM) and the other in which they were considered a “non-responder” (IC50 ≥ 5.0μM, Fig. 1A). To understand the dynamics underlying each drug-response phenotype, we examined pitavastatin sensitivity of two PD-GSC cultures, SN520 and SN503, both of which were isocitrate dehydrogenase 1 (IDH1) wild-type and O6-methylgaunine-DNA methyltransferase (MGMT) unmethylated. The dose titration results revealed distinct susceptibility profiles to pitavastatin treatment. With an IC_{50} of 13.0μM, SN503 was considered a “non-responder”, whereas as SN520 with an IC50 of 0.43μM was labeled a “responder” (Fig. 1A). Next, we investigated the longitudinal response of each PD-GSC culture over a 4-day treatment with DMSO (vehicle control) or pitavastatin at 6.0μM, a dose at which significant decreases in cell viability were observed over the same treatment period (fig. S1). To minimize batch effects, replicate cultures were treated with drug or vehicle over a staggered schedule such that all samples for days 0 (D0), 2 (D2), 3 (D3), and 4 (D4) were collected and processed simultaneously for subsequent flow cytometry, bulk RNA-seq, and scRNA-seq analysis (Fig. 1B). SN520 viability decreased dramatically during treatment between D3 and D4, falling below 90% by day 5 (Fig. 1A). By contrast, over the first three days of pitavastatin treatment, SN503 viability decreased rapidly at a rate that was similar to the kill rate of SN520, but leveled off to approximately 60% for the remainder of the 4-day treatment.

Flow cytometry analysis with annexin V labeling demonstrated that pitavastatin had killed SN520 cells by inducing apoptosis (fig. S2). This result differed from cytometry analysis results of SN503, which did not reveal any dramatic increase in annexin V signal, suggesting that in this PD-GSC culture a mechanism other than apoptosis was responsible for cell death in a small fraction of the population (fig. S2). These findings indicated that the cytotoxic consequences of pitavastatin may vary depending on the composition and characteristics of subpopulations of cells within each PD-GSC culture. Further, the difference in the rate of cell death in both PD-GSC cultures during treatment suggested either the presence of distinct sub-populations of cells with varying susceptibility to pitavastatin, or the possible induction of adaptive responses and cell state transitions across sub-populations within each PD-GSC culture. Subsequent gene set variance analysis (GSVA (*32*)) of bulk RNA-seq profiles was used to generate GBM subtype-specific

bioRxiv preprint doi: https://doi.org/10.1101/2024.02.02.578510; this version posted February 7, 2024. The copyright holder for this preprint (which was not certified by peer review) is the author/funder, who has granted bioRxiv a license to display the preprint in perpetuity. It is made available under aCC-BY-NC-ND 4.0 International license.

enrichment scores, which revealed that subtype compositions of both treated PD-GSC cultures were fairly constant during 4-day vehicle (DMSO) treatment, with SN520 expressing signatures for CL/PN subtypes and SN503 expressing signatures for PN/MES subtypes (Fig. 1C). During pitavastatin treatment, subtype composition of SN520 transitioned from a PN/CL gene signature for the first three days to a predominantly MES subtype on the fourth day of treatment (Fig. 1C). By contrast, the subtype composition of SN503 remained relatively constant throughout pitavastatin treatment. The observed shift in molecular subtypes of SN520 could be explained by either a selection of a pre-existing subpopulation of MES cells or a treatment-induced transition that enabled a subpopulation of surviving cells to escape drug-induced cytotoxicity. Therefore, single-cell-level analysis was required to determine the mechanism driving the subtype change in the bulk cell population. Ultimately, these findings established that despite their similarity in terms of IDH1 mutation and MGMT methylation status, the two PD-GSC cultures exhibited vastly different pitavastatin responses.

Single-cell analysis suggests drug-induced PMT is likely mechanism of acquired pitavastatin resistance in SN520

To further dissect the likely role of sub-population heterogeneity in enabling treatment escape of SN520 and SN503 (Fig. 1B), we performed scRNA-seq profiling of each PD-GSC culture (Chromium, 10X Genomics, Inc.). Following QC of the raw scRNA-seq data (METHODS), a total of 5,402 cells from SN520 and 5,722 cells from SN503 were profiled across all time points (D0, D2, D3, and D4) and treatment conditions (pitavastatin or vehicle control). Batch-integration with Harmony (*33*), dimensionality reduction, and visualization with uniform manifold approximation and projection (UMAP, (*34*)) of the integrated scRNA-seq data revealed distinct pitavastatin-specific transcriptional responses across the two PD-GSCs (Fig. 1D). In SN520, we observed time-dependent clustering of cells, indicating a coordinated transcriptional response to pitavastatin. By contrast, there was considerable overlap between pitavastatin-treated SN503 cells from all time points (Fig. 1D). We quantified net temporal shifts in transcriptomic states of the cells, or lack thereof, using Wasserstein distance, which quantifies dissimilarity between two high-dimensional distributions (*35*). Drug treatment caused the SN520 cells to become progressively dissimilar from the preceding state over time, unlike vehicle-treated cells. By contrast, there was a slight increase in Wasserstein distance in drug-treated SN503 cells between D2 and D3, but not between D3 and D4 samples (Fig. 1E). Given the distinct response patterns of the two PD-GSCs, subsequent scRNA-seq analysis was performed on a patient-specific basis, (Fig. 2A, B). UMAP plots organized cells within each PD-GSC into two main groups, defined by

bioRxiv preprint doi: https://doi.org/10.1101/2024.02.02.578510; this version posted February 7, 2024. The copyright holder for this preprint (which was not certified by peer review) is the author/funder, who has granted bioRxiv a license to display the preprint in perpetuity. It is made available under aCC-BY-NC-ND 4.0 International license.

treatment with either pitavastatin or vehicle control. Pitavastatin-treated SN520 cells organized along treatment time whereas pitavastatin-treated SN503 cells from different time points overlapped with one another in the gene expression space as captured by the UMAP embeddings.

Interestingly, GSVA enrichment scoring (fig. S3) showed that while the relative proportions of cells for each molecular subtype (i.e., CL, PN, MES) was fairly consistent in vehicle control, the 4-day pitavastatin treatment of SN520 cells showed a dramatic increase in the proportion of cells of the MES subtype (Fig. 2C). In stark contrast and consistent with bulk RNA-seq analysis, the SN503 culture did not exhibit any significant change in subtype composition with either vehicle or pitavastatin treatment (Fig. 2D and Fig. 1C). Generally, the trends observed at the single-cell level, i.e., a dramatic increase in MES subtype in SN520 and a mixture of molecular subtypes in SN503, were reflected at the bulk-level (Fig. 1C). Furthermore, similar patterns in proportions of GSC subpopulations were observed when cells were annotated according to the more recently defined cell-state classification of GBM tumor cells (*36*) (fig. S4).

Cytometry analysis confirmed findings from scRNA-seq analysis that pitavastatin treatment of SN520 resulted in an increase in the proportion of CD44+ (MES) cells from 28.2% to 65.35%, and a simultaneous decrease in CD133+ (PN) cells from 52.7% to ~1%. Of note, SN520 had a sizeable (35.3%) proportion of CD133+/CD44- PN cells, which were nearly eliminated by D4 (Fig. 2E), likely due to a combination of treatment-induced killing and a transition of surviving cells to a MES state. By contrast, pitavastatin treatment did not cause a change in the proportion of CD44+ cells in SN503 (87% on D1 to 85.11% on D4, Fig. 2F). The significant decrease in the relative proportion of CD133+ cells within SN503 (from 38.1% on D1 to 9.51% on D4), especially over the first two days of treatment, was likely due to pitavastatin-induced killing of a susceptible PN subpopulation (*9*). Interestingly, the relative proportion of CD133+/CD44- PN cells (1.41%) within SN503 was negligible; pitavastatin sensitivity appeared to be associated with a CD133+/CD44+ sub-population that was in higher abundance (36.7%).

To differentiate between selection and differential proliferation as opposed to cell type conversion (PMT) as the mechanism responsible for the observed shifts in subtype composition, we used canonical cell cycle gene expression signatures to score each cell (METHODS) and found that only small proportions of cells within each PD-GSC culture were in the S or G2/M phase regardless of treatment context (fig. S5). Consistent with this finding, cytometry-based DNA

bioRxiv preprint doi: https://doi.org/10.1101/2024.02.02.578510; this version posted February 7, 2024. The copyright holder for this preprint (which was not certified by peer review) is the author/funder, who has granted bioRxiv a license to display the preprint in perpetuity. It is made available under aCC-BY-NC-ND 4.0 International license.

quantification of individual cells confirmed that only a small proportion of cells across both PD-GSCs were actively proliferating during pitavastatin treatment (fig. S6). Theoretical calculations based on cell division rate and treatment duration (fig. S7), as well as the homogeneity of CNV states pre- and post-treatment of both PD-GSCs (Fig. 2G, H) both independently suggested that cell subtype transitions of surviving SN520 cells, rather than a natural selection and expansion of a subclone, was responsible for the observed treatment-induced changes in subtype composition and phenotypic characteristics. Finally, overall drug sensitivity of surviving SN503 cells remained relatively unchanged post-pitavastatin treatment for ~30 days (Fig. 2I; paired t-test p-value = 0.348). In stark contrast, there was significant 2.4 log2-fold increase in IC_{50} of surviving SN520 cells from 0.42 μM to 2.24 μM, which was sustained over 100 days (Fig. 2I; paired t-test p value = 1.526e-05), demonstrating the long-term functional consequences of drug-induced PMT.

Characterization of transcriptional states of PD-GSCs reveals multiple mechanisms of primary and acquired resistance

Dimensionality reduction with PCA and subsequent Louvain clustering (METHODS) organized the 5,402 SN520 cells into 14 clusters (Fig. 3A, B) and the 5,722 SN503 cells into 12 clusters ($cl_{503/520}$-*i*; Fig. 3C, D). As expected, the SN520 Louvain clusters were predominantly comprised of either vehicle- or pitavastatin-treated PD-GSCs (Fig. 3C). By contrast, several SN503 Louvain clusters contained a mix of both vehicle- and drug-treated cells (Fig. 3D). Below we summarize findings based on pathway enrichment analysis of differentially expressed genes (DEGs, fig. S8) within each Louvain cluster (Fig. 3E). A more detailed description is included in the Supplementary Materials.

SN520 Clustering & Enrichment. Consistent with the mechanism of action of pitavastatin, gene set enrichment analysis (GSEA, tables S1-S2) revealed that within two days upon initiation of treatment SN520 cells differentially regulated cholesterol homeostasis, biosynthesis, and maintenance, as well as MTORC1 signaling. Cells from D3 and onwards the cells differentially regulated stress response genes including unfolded protein response, protein secretion, P53 pathway, and apoptosis. Closer examination of those Louvain clusters enriched with apoptotic gene signatures (cl_{520}-4, cl_{520}-6, cl_{520}-7, cl_{520}-12, and cl_{520}-13) revealed that 4 of the 5 clusters contained cells from all molecular subtypes, indicating that drug sensitivity was not necessarily subtype-specific (fig. S8). Concomitantly, the killing of susceptible cells alone does not explain the coordinated change in subtype composition of SN520, given that MES subtype cells were approximately 2% of the original population, whereas they comprised 94% of the total population

bioRxiv preprint doi: https://doi.org/10.1101/2024.02.02.578510; this version posted February 7, 2024. The copyright holder for this preprint (which was not certified by peer review) is the author/funder, who has granted bioRxiv a license to display the preprint in perpetuity. It is made available under aCC-BY-NC-ND 4.0 International license.

on D4 (Fig. 2C), when 80% of cells were killed by pitavastatin treatment (Fig. 1A). Interestingly, upregulation of both apoptosis and EMT genes across subpopulations of drug-treated D4 cells (cl_{520}-6, cl_{520}-7) was consistent with simultaneous induction of these pathways by TGFβ during tumor formation and progression, with cell fate being dependent on cell-cycle phase (*37*, *38*). In this case, cl_{520}-6 and cl_{520}-7 cells were in G1/S phase, suggesting that SN520 cells escaped apoptosis by transitioning into the MES subtype (fig. S8).

SN503 Clustering & Enrichment. Although there were fewer DEGs in SN503 as compared to SN520 (Fig. 3F), the Louvain clusters of pitavastatin-treated SN503 cells did bear similarity to SN520 clusters with regard to differential regulation of certain pathways, including cholesterol homeostasis, fatty acid metabolism, MTORC1 signaling, androgen response, and unfolded protein response (tables S3 – S4). However, the differential expression patterns were distinct between the two PD-GSCs. For instance, pitavastatin-treated SN503 cells did not cluster by treatment time; instead, cells from all time points grouped together across multiple Louvain clusters (Fig. 3D, E) characterized by upregulation of oxidative phosphorylation (OXPHOS, Fig. 3G, table S3), which has been associated with drug resistance in tumor cells (*39–42*). Moreover, only a small proportion of pitavastatin-treated SN503 cells differentially regulated EMT-associated genes (cl_{503}-0 and cl_{503}-5) (Fig. 2, Fig. 3E). Furthermore, only two Louvain clusters differentially regulated apoptotic genes (cl_{503}-0 and cl_{503}-10), both of which contained cells from all three molecular subtypes (fig. S8). Thus, the differential enrichment of apoptotic signatures was consistent with responder and non-responder phenotypes of the two PD-GSCs, suggesting variable susceptibility of sub-populations with a greater proportion of pitavastatin sensitive cells in SN520 as compared to SN503. These findings suggested that different regulatory mechanisms were likely responsible for the distinct differential expression patterns of key pathways, as well as the responder and non-responder phenotypes of SN520 and SN503, respectively.

Inference and simulation of the dynamics of transcriptional regulatory networks identify mechanisms driving cell-state changes and intervention strategies

We applied single-cell SYstems Genetics Network AnaLysis (scSYGNAL) framework to uncover the transcriptional regulatory networks (TRNs, (*43*, *44*)) responsible for driving the distinct transcriptome responses of the two PD-GSCs. Briefly, Mechanistic Inference of Node Edge Relationships (MINER), an algorithm within the scSYGNAL framework, was used to identify modules of genes (regulons) that were co-regulated differentially in response to treatment across sub-populations of cells (*45*, *46*). Further, using the transcription factor binding site database (*47*)

bioRxiv preprint doi: https://doi.org/10.1101/2024.02.02.578510; this version posted February 7, 2024. The copyright holder for this preprint (which was not certified by peer review) is the author/funder, who has granted bioRxiv a license to display the preprint in perpetuity. It is made available under aCC-BY-NC-ND 4.0 International license.

and the Framework for Inference of Regulation by miRNAs (FIRM, (*48*)), scSYGNAL implicated specific TFs and miRNAs in mechanistically co-regulating genes of all regulons. Post-processing of the resulting TRNs using MINER (*49*) clustered regulons with similar activity profiles across subpopulations of cells into transcriptional programs ($Pr_{503/520}$-*i*) and clustered single cells with similar program activity profiles into distinct transcriptional states ($St_{503/520}$-*i*). Here onwards we will refer to the TRNs for each PD-GSC as scSYGNAL-520 and scSYGNAL-503.

scSYGNAL-520 modeled the influence of 109 TFs and 505 miRNAs in mechanistically regulating 1,668 genes across 572 regulons that organized into 19 transcriptional programs and were differentially active across 17 transcriptional states (Fig. 4A, tables S5-S6). Strikingly, nearly every transcriptional program was enriched for genes that have been shown to be essential to GSC survival (table S7, (*50*)). GSEA revealed that many pathways identified within Louvain clusters were recapitulated by programs (Fig. 3G, table S8). For instance, Program 0 (Pr_{520}-0) – the largest program consisting of 169 regulons, was enriched for genes associated with cellular stress responses, including unfolded protein response, androgen response, p53 pathway, and apoptosis. Pr_{520}-1, the second largest program (61 regulons) was enriched for cholesterol homeostasis and MTORC1 signaling. Pr_{520}-2 (proliferation), Pr_{520}-5 and Pr_{520}-6 (TNFα signaling via NFκB) showed variable activity in states enriched with vehicle-treated cells, but were uniformly underactive in states enriched with pitavastatin-treated cells (Fig. 4A). Only four states (St_{520}-0 – St_{520}-3) were enriched for D3 and D4 pitavastatin-treated cells (Fig. 4B), suggesting that they might represent drug resistant states adopted by the surviving subpopulation of cells to avoid pitavastatin-induced killing. Furthermore, when transcriptional states were rearranged with respect to their predominant treatment condition, program activities increased (nearly) monotonically over the course of treatment, which suggested that treatment-induced state transitions occurred through continuous rather than discrete changes in expression in SN520 (Fig. 4C, fig. S9).

scSYGNAL-503 modeled the regulation of 1,875 genes by 114 TFs and 507 miRNAs across 420 regulons, organized into 21 distinct transcriptional programs, whose activity profiles stratified SN503 cells into 17 transcriptional states (Fig. 4A bottom heatmap, tables, S9-S10). Like SN520, a large portion of these programs were enriched with essential genes for GSC survival (table S11, (*50*)). Several programs were similar to those identified in SN520, including Pr_{503}-13 (cholesterol homeostasis, MTORC1 signaling and fatty acid metabolism), Pr_{503}-9 and Pr_{503}-10 (stress responses, including vesicle-mediated transport, unfolded protein response, and p53 pathway).

bioRxiv preprint doi: https://doi.org/10.1101/2024.02.02.578510; this version posted February 7, 2024. The copyright holder for this preprint (which was not certified by peer review) is the author/funder, who has granted bioRxiv a license to display the preprint in perpetuity. It is made available under aCC-BY-NC-ND 4.0 International license.

In contrast to SN520, many SN503 programs were uniquely enriched in distinct processes, including WNT/β-catenin and KRAS signaling (Pr_{503}-18, Fig. 4F, table S12). Unlike SN520, D3 and D4 pitavastatin-treated SN503 cells co-clustered in significant proportions with untreated and vehicle-treated cells across >75% of the 17 states, suggesting that a large number of SN503 cells may have been in pitavastatin-resistant states even prior to drug exposure (Fig. 4C). Interestingly, multiple states included pitavastatin-treated cells from all time points, including seven states in which the drug-treated cells represented >50% of all cells (Fig. 4B). The seven transcriptional states were distinct in their activity patterns of some programs, including Pr_{503}-4 (apoptosis, EMT, IL6/JAK/STAT3 signaling), which was overactive in St_{503}-5, St_{503}-6, and St_{503}-10; and Pr_{503}-10 (MTORC1 signaling, hypoxia, and unfolded protein response), which was overactive in St_{503}-10 and St_{503}-11. The heterogeneous activity patterns of these programs, which were enriched for processes linked to chemotherapeutic resistance (*51*), suggests that multiple mechanisms likely contributed to pitavastatin resistance in SN503.

Core TF-TF interaction networks governing PD-GSC response to pitavastatin.

From the TRN of each PD-GSC, we extracted a network of TF-TF interactions among the 114 and 109 TFs implicated in mediating the pitavastatin responses of SN503 and SN520, respectively. We derived a “core” network of TF interactions, i.e., the largest network of interconnected TFs, to investigate how transcriptional regulatory mechanisms contributed to PMT and pitavastatin resistance (Fig. 4D). Each directed TF-TF interaction was categorized as activating or repressing based on positive or negative pairwise correlation of expression levels between two TFs, respectively. The topology of the core TF network for each PD-GSC was distinct (METHODS), with 56 interactions (edges) among 31 TFs (nodes) in scSYGNAL-520 and only 13 interactions connecting 15 TFs in scSYGNAL-503 (Fig. 4E, F). Multiple TFs in the core scSYGNAL-520 TF network have been linked to response-relevant processes including EMT, cell differentiation, adaptive responses, and stem-cell maintenance (table S13). Nine TFs were common between the core networks (overlap p-value: 9.44e-05), including ARID5A, ATF3/4, MEOX2, SOX9, XBP1, and HEY1, a Notch signaling regulator. TFs unique to the core scSYGNAL-503 network included DDIT3, MAFF, STAT3, and ID4, which have been implicated in multiple GBM-relevant processes, (table S13). Notably among these TFs, ID4 has also been shown to play a role in the pathogenesis of GBM, driving tumor-initiating cell formation by increasing two key cell-cycle and differentiation regulatory molecules – cyclin E and Jagged 1 (*52*). These findings suggest that the core networks captured TF-regulation that play central roles in GBM and gliomas in general.

bioRxiv preprint doi: https://doi.org/10.1101/2024.02.02.578510; this version posted February 7, 2024. The copyright holder for this preprint (which was not certified by peer review) is the author/funder, who has granted bioRxiv a license to display the preprint in perpetuity. It is made available under aCC-BY-NC-ND 4.0 International license.

Trajectory analysis and network simulations uncover mechanisms of primary and acquired resistance

Using Monocle3 we discovered that pseudotemporal ordering of SN520 cells correlated with treatment duration and concomitant drug-induced PMT (Pearson correlation coefficient r = 0.723). We observed similar agreement between treatment duration and inferred trajectories from multiple RNA velocity analyses (Fig. 5A, fig. S10) (*53*, *54*), as velocity vectors pointed towards 4-day treated cells. In parallel, we calculated the critical transition index (I_c), a quantitative metric of the high-dimensional state of a system that predicts whether a cell population is undergoing a state transition (higher I_c values) or if it has reached some stable attractor state (lower I_c values) (*55*). I_c values of SN520 decreased during drug treatment but remained relatively constant in the vehicle control (Fig. 5B), indicating that pitavastatin had driven the entire PD-GSC population into a predominantly drug-resistant MES subtype attractor state. By contrast, pseudotemporal ordering of SN503 cells did not correlate with treatment time (Pearson correlation coefficient r = –0.0167,) and was associated with high I_c values throughout the course of the experiment for both vehicle control and drug treatment, likely driven by the higher heterogeneity of the cells. Consistently, these GSCs exhibited a rather turbulent vector field where RNA velocities projected into multiple directions (Fig. 5A). Modeling concerns associated with pseudotime and trajectory inference analysis notwithstanding, e.g., hyperparameter optimization (*56*, *57*), the pseudotime and criticality analyses demonstrated stark contrast between the responses of the two PD-GSCs; SN520 exhibited concerted pitavastatin-induced state transitions, relaxing into a regulated state, while SN503 exhibited a seemingly disorganized response without concerted transition of all cells into an attractor state.

To identify putative drivers of treatment response, we performed LOESS regression and rank ordered TFs with respect to timing of peak expression along the pseudotime trajectories and uncovered a distinct sequence of changes in the activity of multiple TFs in each PD-GSC population (Fig. 5C). Within SN520, multiple TFs previously associated with PMT in GBM (e.g., ATF3, CREB, and NFE2L2) positively correlated with pseudotime trajectory (table S13 – Moran's I value). Notably, the rank order of TFs in SN520 was quite different from previously proposed sequence of transcriptional events driving PMT (*58*), which highlights the diversity of regulatory mechanisms that have been implicated in driving EMT in multiple cancers (*59*, *60*). As expected, we did not observe temporal sequence of changes in expression levels of TFs across SN503 cells (Fig. 5C, fig. S11, table S13).

bioRxiv preprint doi: https://doi.org/10.1101/2024.02.02.578510; this version posted February 7, 2024. The copyright holder for this preprint (which was not certified by peer review) is the author/funder, who has granted bioRxiv a license to display the preprint in perpetuity. It is made available under aCC-BY-NC-ND 4.0 International license.

In addition, we investigated the consequence of differential expression patterns of TFs by examining, along pseudotime trajectories, the dynamic activity patterns of transcriptional programs that they regulated (Fig. 5D, fig. S11). Activity of the stress-response-associated programs (Pr_{520}-0) increased along the pseudotime trajectory of SN520 cells, implicating 80 associated TFs, including ATF3, ATF4, CREB3, CREB5, JUN, KLF4, MYC, SOX4/9, and TCF4. In the case of SN503, we identified multiple treatment-activated programs for key processes (Fig. 4C) including unfolded protein response and OXPHOS (Pr_{503}-9 and Pr_{503}-10), cholesterol regulation (Pr_{503}-4) and EMT (Pr_{503}-5 and Pr_{503}-13) that showed upregulated gene expression relative to the untreated control condition (Fig. 5E). Importantly, scSYGNAL-503 had accurately identified TFs that have been mechanistically implicated in regulation of these processes, such as AR, FOS, MYC, TP53, and E2F7 for Pr_{503}-9 and Pr_{503}-10 (*61*).

Ensemble modeling and analysis of GSC states via simulated TF-TF network dynamics

We performed *in silico* perturbations on the core TF-TF networks using the random circuit perturbation (RACIPE) algorithm (*62–64*) to identify transcriptional regulatory mechanisms that governed pitavastatin-induced cell state changes across the two PD-GSCs (Fig. 4D, E). RACIPE was originally developed to investigate EMT circuits in cell development and other cancers by creating an ensemble of dynamic models based on ordinary differential equations and Hill function kinetics (*65–67*). First, we tested whether the TF-TF network model for each PD-GSC could accurately predict their observed pitavastatin-induced cell states using untreated (D0) TF expression levels to initialize the network. By performing 1,000 RACIPE simulations, we determined that the simulated stable steady states were statistically similar to the observed cell states of each PD-GSC on D4 of pitavastatin treatment (Fig. 6A, B, fig. S12).

Next, we investigated how the core TF network contributed to phenotypic plasticity by determining the range of steady states that could emerge from each network topology. We simulated 10,000 distinct models (i.e., parameter sets) across 100 randomly selected initial conditions resulting in an ensemble of 1 million simulations for each PD-GSC population, which was sufficient to yield convergent solutions (fig. S13 (*62–64*)). Based on pairwise Euclidean distances (METHODS) and hierarchical clustering, all simulated states generated by the core TF network for SN520 clustered into four distinct steady states (Fig. 6C)**.** The simulated states stratified along the first principal component, recapitulating a continuum of progression from a PN to MES state (Fig. 6C). Pairwise comparisons of mean expression profiles of the core network TFs demonstrated that the simulated states were statistically similar to experimentally observed PD-GSC states (Fig. 6C, fig.

bioRxiv preprint doi: https://doi.org/10.1101/2024.02.02.578510; this version posted February 7, 2024. The copyright holder for this preprint (which was not certified by peer review) is the author/funder, who has granted bioRxiv a license to display the preprint in perpetuity. It is made available under aCC-BY-NC-ND 4.0 International license.

S12). Supervised classification using random forest analysis further revealed that ATF3/4, CEBPG, and HES1 contributed the most to distinguishing the four simulated states (Fig. 6C), which mirrored expression behavior across experimental data for SN520 (Fig. 6D).

RACIPE simulations for SN503 also yielded four distinct stable steady states that did not show a gradient in PCA space as in the case of SN520 simulated states (Fig. 6E). Three of these states were similar to two experimentally observed PD-GSC states (Fig. 6F) associated with elevated expression of SOX4, SOX9, SOX11, HEY1, and ID4 (simulated states 3 and 4 and experimental state 3, fig. S12), or elevated expression of ATF3, ATF4, and FOS (simulated states 1 and 3 and experimental state 4, fig. S12). The experimentally observed states not identified by RACIPE simulations were associated with elevated expression of MEOX2, MAFF, and ARID5A, which were "root" nodes, i.e., TFs without any upstream regulators in the context of the model. Consequently, expression of these TFs in the RACIPE simulations was dependent upon the randomly selected initial conditions. However, the subset of simulations in which MEOX2, MAFF, and ARID5A had elevated initial conditions generated states that were indeed similar to experimentally observed states ES_{503}-1 and ES_{503}-2 (fig. S12). Finally, to distinguish the four SN503 PD-GSC states, random forest analysis identified MEOX2, MAFF, and ARID5A as the most important TFs, followed by ATF3, SOX9, and SOX11 (fig. S12). Interestingly, all of these TFs have previously been implicated in tumor stemness, progression, invasiveness or resistance, suggesting multiple mechanisms may have contributed to pitavastatin resistance in SN503 (table S13).

In silico network perturbations implicate specific TFs in mechanistically driving treatment-induced cell state transitions and drug resistance in PD-GSCs

After benchmarking the random forest models as 85% and 90% accurate in predicting cell states of SN520 and SN503, respectively (fig. S14), we used them in perturbation simulations to identify mechanistic drivers of treatment response of each PD-GSC. Specifically, we performed an additional 1 million RACIPE simulations to model the consequence of 95% knockdown in each TF within the core network on treatment-induced change in the relative abundance of each of the four steady states for the two PD-GSCs. (fig. S15). This analysis predicted that knockdowns in each of ten TFs, viz., ATF4, IRF1, NFE2L2, CREB3, XBP1, ARID5A, SMAD1, CREB5, CEBPG, and ATF3, would result in significant reduction in the relative abundance of simulated states with large subpopulations of MES subtype cells in SN520 (Fig. 6G). Notably, all ten TFs have been implicated in driving EMT across different cancers, including GBM (table S13). RACIPE

bioRxiv preprint doi: https://doi.org/10.1101/2024.02.02.578510; this version posted February 7, 2024. The copyright holder for this preprint (which was not certified by peer review) is the author/funder, who has granted bioRxiv a license to display the preprint in perpetuity. It is made available under aCC-BY-NC-ND 4.0 International license.

simulations predicted that decrease in the proportion of MES subtype-associated cell states in SN503 was likely through perturbations in just two TFs, namely SOX9 and SOX11 (fig. S15) both of which were also implicated in driving PMT (table S13).

siRNA knockdowns of TFs validate core TF networks

We tested RACIPE predictions by investigating whether siRNA (Dharmacon™) knockdown of TFs during pitavastatin treatment would block PMT leading to synergistic increase in PD-GSC killing. Indeed, knockdowns in nine TFs (5/10 predicted), including ATF3, IRF1, CREB3, CREB5, and CEBPG, significantly potentiated pitavastatin killing of SN520 (Fig. 6G). Notably, increased cell death of SN520 was observed with *sequential treatment* with pitavastatin followed by siRNA. Co-administering siRNA and pitavastatin also achieves a sequential intervention, since siRNAs take approximately two days to achieve maximal knockdown of target protein levels after transfection (Dharmacon™). Potentiation of killing was not observed with *simultaneous treatment*, which was achieved by pre-treatment of cells with siRNA 2 days prior to administering pitavastatin (Fig. 6G). These findings showed that dynamic induction of TF activity by pitavastatin was essential for potentiation of SN520 killing by siRNA-mediated TF knockdown. In stark contrast, none of the TF knockdowns had any consequence on viability of SN503, in sequential or simultaneous treatment contexts. Altogether, the experimental findings corroborated the roles of nine TFs implicated by scSYGNAL and RACIPE analysis in driving PMT, thereby conferring pitavastatin resistance in SN520, but not in SN503, wherein a large fraction of the cell population was in a drug resistant MES state, even prior to drug treatment. As an alternative approach, we identified 24 additional TFs by MINER as important for mechanistically upregulating putative resistance mechanisms, including OXPHOS (Fig. 2G, tables S3, S12), and discovered that knocking down four TFs (HEY2, POU3F4, PRDM4, and PEG10) indeed potentiated pitavastatin-induced killing of SN503, likely by disrupting one or more primary resistance mechanism(s) in a sequence-dependent manner (Fig. 6H).

Trajectories towards acquired resistance expose vulnerabilities to secondary drugs

Finally, we investigated whether knowledge of mechanistic drivers of PMT could enable rational selection of a second drug that could potentiate the action of pitavastatin. Using Open Targets (*68*), we identified eight drugs that targeted TFs and genes associated with pitavastatin-induced PMT trajectories in SN520. We hypothesized that pitavastatin-induced cell state changes place cells in transitional states that may expose new vulnerabilities that could be targeted by secondary drugs. We selected vinflunine, a vinca alkaloid that binds to tubulin and inhibits microtubule

bioRxiv preprint doi: https://doi.org/10.1101/2024.02.02.578510; this version posted February 7, 2024. The copyright holder for this preprint (which was not certified by peer review) is the author/funder, who has granted bioRxiv a license to display the preprint in perpetuity. It is made available under aCC-BY-NC-ND 4.0 International license.

polymerization, thereby inducing G2/M arrest and ultimately apoptosis. Originally developed to treat advanced or metastatic transitional cell carcinoma of the urothelial tract (*69*), vinflunine has been tested in multiple Phase III trials for many cancers, used as a likely potentiator of anti-cancer effects of other drugs (*70*). Based on vinflunine's mechanism of action, we identified multiple regulons containing tubulin-related genes (for example, SN520 regulons R_{520}-0 and R_{520}-43; SN503 regulons R_{503}-19, R_{503}-38, and R_{503}-52). In SN520, the activity for R_{520}-0 and R_{520}-43 increased significantly in response to pitavastatin (Fig. 7A). By contrast, pitavastatin-induced upregulation of tubulin-associated regulons was varied across in SN503, with only R_{503}-19 showing consistent over activity across all time points. R_{503}-38 showed significantly higher activity in pitavastatin-treated cells relative to vehicle-treated, with maximal activity on D3. Finally, R_{503}-52 activity levels were slightly higher relative to vehicle control (Fig. 7B). The ability of vinflunine to block pitavastatin-induced cell state transitions was investigated in three experimental designs, one in which both drugs were added simultaneously and the other two in which vinflunine was added at 24 or 48hrs after initiation of pitavastatin treatment to match the timing when pitavastatin-treatment induced the highest activity of tubulin regulons (Fig. 7C). The efficacy of the drug combinations were compared to outcome of treatments of PD-GSCs with each individual drug.

Sequential treatments with pitavastatin followed by vinflunine had synergistic effect on killing of the two PD-GSCs. Specifically, sequential treatment of pitavastatin followed by vinflunine resulted in significant lower cell viability relative to pitavastatin treatment alone (Fig. 7D) and a 5.92- and 1.6-fold decrease of IC_{50}, compared to vinflunine treatment alone (fig. S16) in SN520 and SN503, respectively. The relative efficacy of sequential treatment with the two-drug combination varied significantly across other PD-GSCs (table S14), with the combination being more effective on pitavastatin responder (SN533 and SN575) than non-responder PD-GSCs (SN517 and SN521) (fig. S16). The poor efficacy of vinflunine on SN503 and other non-responder PD-GSCs is likely because pitavastatin did not induce a coordinated response that placed cells in a vulnerable state from which we predicted the utility of vinflunine based on the transcriptional network. Thus, the coordinated cell-state changes induced by pitavastatin killing of susceptible cells in the responder PD-GSCs pushed the surviving cells along PMT trajectories with generic and patient-specific characteristics, thereby exposing novel vulnerabilities that significantly potentiated increased killing upon sequential treatment with vinflunine.

DISCUSSION

bioRxiv preprint doi: https://doi.org/10.1101/2024.02.02.578510; this version posted February 7, 2024. The copyright holder for this preprint (which was not certified by peer review) is the author/funder, who has granted bioRxiv a license to display the preprint in perpetuity. It is made available under aCC-BY-NC-ND 4.0 International license.

Inherent plasticity and heterogeneity of GSCs are implicated as underlying reasons for the high rate of GBM recurrence, which often manifest as an even more aggressive and drug-resistant MES subtype (*8*–*10*). Understanding the mechanisms of primary resistance and trajectories along which GSCs undergo adaptive subtype transitions to acquire resistance are both critical for formulating treatment regimens to prevent recurrence of aggressive and drug resistant GBM (*7*, *71*). In this study, we report five main findings that shed insight into the underlying mechanisms of phenotypic plasticity of PD-GSCs: 1) distinct population structures distinguished two PD-GSCs with acquired (SN520) and primary (SN503) resistance phenotypes, 2) distinct TF network topologies were associated with the two GSC phenotypes, 3) TF network topology was a key determinant of treatment-induced change in the population structure of PD-GSCs, 4) TF network topology inferred from scRNA-seq enabled predictions of underlying mechanistic drivers of primary and acquired resistance, including response trajectories, 5) disruption of primary resistance potentiated killing of non-responder PD-GSCs, and 6) treatment-induced trajectories through which PD-GSCs acquired resistance, exposed vulnerabilities to sequential interventions (siRNA KD of TFs or a secondary drug) targeting transcriptional programs mechanistically associated with cell state transitions.

Primary resistance of SN503 was likely due to a larger pre-existing subpopulation of MES subtype cells, identified by both scRNA-seq and flow cytometry (Fig. 2C-F), with elevated expression of OXPHOS and fatty acid metabolism (Fig. 5E) and high activity of WNT/β-catenin signaling pathway genes in Pr_{503}-18 (Fig. 4F) (*7*, *72*, *73*). Hence, pitavastatin treatment was less effective on SN503 and failed to trigger a coordinated transcriptional response across the population of surviving cells in this PD-GSC. By contrast, a smaller proportion of SN520 cells were of the MES subtype (Fig. 2C, D) and activity of programs associated with known treatment-resistance mechanisms was low. As a result, pitavastatin killed most SN520 cells, triggering coordinated transcriptional responses across the surviving PD-GSCs, driving their transition into a MES subtype cell state that was more than 5-times resistant to pitavastatin (Fig. 2I). Flow cytometry using apoptosis/subtype-specific markers, CNV inference, and theoretical calculations based on cell division rates all demonstrated that pitavastatin-induced cell state and phenotypic transitions were mediated by epigenetic mechanisms and not clonal selection. We also ruled out the hypothesized role of histone deacetylase (HDAC) inhibition activity of statins as a likely mechanism by which pitavastatin treatment might have induced large scale change in gene expression across the two PD-GSCs (Supplementary Text and table S15). Further, the core TF-TF networks inferred from scSYGNAL analysis were determined by RACIPE simulations as

bioRxiv preprint doi: https://doi.org/10.1101/2024.02.02.578510; this version posted February 7, 2024. The copyright holder for this preprint (which was not certified by peer review) is the author/funder, who has granted bioRxiv a license to display the preprint in perpetuity. It is made available under aCC-BY-NC-ND 4.0 International license.

548 sufficient to generate the observed heterogeneity and treatment-induced cell state changes of the
549 two PD-GSCs. Our findings showed that the TF-TF network topology was likely a key factor in
550 determining the trajectory and potential endpoint(s) of cell-state transitions in response to drug
551 treatment or perturbation. The sparse network of SN503 generated multiple resistant states that
552 were distinct from each other. Interestingly, SN503 contained a large number of smaller
553 interconnected networks of two or three TFs that were not connected to the core network (Fig.
554 4F). This finding was consistent with the lack of concerted cell state changes in the non-responder
555 PD-GSC and limited information flow throughout the core TF network due its sparse and
556 disconnected topology. The interconnected network of SN520, by contrast, generated a gradient
557 of cell states along a PN-to-MES axis offering a plausible explanation as to why GSCs manifest
558 a gradient of resistant states across a range of drugs (*9*). It is important to note that the core TF-
559 TF network models are static representations of the sum of interactions that drove pitavastatin-
560 induced responses of each PD-GSC. By performing dynamic simulations across a wide range of
561 initial conditions and kinetic parameters and experimentally validating TF targets via siRNA
562 perturbations, we demonstrated that many of these TFs were mechanistically responsible for
563 driving the two PD-GSCs into various states observed experimentally. Together, our findings
564 provide novel perspective on how patient-to-patient variation in the roles of TFs and the topology
565 of their interactions can have profound consequences in driving PMT, likely influencing the rate
566 of GBM progression, recurrence, and metastasis as tumors of MES subtype (*27*, *74*).
567
568 By killing a large proportion of cells, pitavastatin treatment triggered a core network of TFs to act
569 sequentially and drive coordinated cell-state transitions across the surviving population of SN520.
570 In so doing, pitavastatin treatment may have generated a bottleneck effect by channeling the
571 surviving SN520 cells along few trajectories, thereby transiently exposing vulnerabilities in
572 associated transcriptional programs across a large segment of those surviving cells, before they
573 transitioned to the MES subtype and acquired a drug-resistant phenotype. Similar constraining
574 effects on GSC plasticity, i.e., fewer cell-state transitions have been observed and attributed to
575 hypoxic micro-environments, unlike the larger number of stochastic cell state transitions that occur
576 under normoxic conditions (*75*). Our findings demonstrate that such constraints on plasticity
577 makes the GSC population less heterogeneous and more vulnerable to siRNAs and drugs
578 targeting transiently activated programs that mechanistically coordinate the cell state transitions.
579 Taken together, these results suggest that the bottleneck effect generated by drug treatment can
580 be exploited to minimize or prevent drug-induced transitions and therapy escape of GSCs.
581

bioRxiv preprint doi: https://doi.org/10.1101/2024.02.02.578510; this version posted February 7, 2024. The copyright holder for this preprint (which was not certified by peer review) is the author/funder, who has granted bioRxiv a license to display the preprint in perpetuity. It is made available under aCC-BY-NC-ND 4.0 International license.

Notably, the timing of the secondary intervention with siRNAs was critical, with efficacy of potentiation observed only *after* cell-state transitions had been triggered by pitavastatin treatment. The combinatorial interventions were ineffective in potentiating killing when the siRNA effects manifested simultaneously with pitavastatin treatment concurrently (Fig. 6G, H). These findings illustrate the importance of tailoring not just the specific combination of interventions, but also the order and timing of longitudinal treatment schedules based on mechanistic understanding of the causal sequence of events targeted by each individual intervention. Similar benefits from modeling cell state transitions and characterizing trajectories have also been reported in PDGF-driven GBM mouse models. Specifically, the integration of mathematical models that account for the presence of radiosensitive and radioresistant tumor cell states as well as the rate at which state transitions occurred led to an optimized radiotherapy scheduling that improved survival rates of mice (*76*, *77*).

Combination treatment with vinflunine was effective to varying degrees across other PD-GSCs that were also sensitive to pitavastatin (SN533 and SN575), but was less effective in pitavastatin-resistant PD-GSCs (SN503, SN517 and SN521). This finding suggests that cytotoxic effects of pitavastatin were likely important to expose vulnerabilities, and that the mechanism of killing by pitavastatin and resulting trajectories of escape were likely similar across some of these PD-GSCs. However, variable susceptibilities of PD-GSCs to vinflunine explain why an *N = 1* approach is necessary to uncover patient-specific characteristics and tailor regimen to their unique PMT trajectories (fig. S17, (*58*)).

The partial generalizability of pitavastatin-vinflunine combination treatment to other pitavastatin-sensitive PD-GSCs, further suggests that subgroups of patients might share transcriptional regulatory network topologies that drive their tumor cell state transitions along similar trajectories. If this hypothesis is confirmed by analyzing a larger number of PD-GSCs across a diverse range of drug treatments, then stratifying patients based on similar network topologies, instead of steady states of tumor cells, may identify a finite number of topology-matched combinatorial interventions for personalized treatment of most patients (*2*, *3*, *36*).

The causal and mechanistic regulatory influences captured at single-cell resolution in the scSYGNAL network provides a generalizable approach for formulating *N = 1* patient-tailored drug regimens and treatment schedules. Remarkably, we discovered that more than the composition of initial tumor cell states, mechanistic understanding of the topology of the core TF-TF network

bioRxiv preprint doi: https://doi.org/10.1101/2024.02.02.578510; this version posted February 7, 2024. The copyright holder for this preprint (which was not certified by peer review) is the author/funder, who has granted bioRxiv a license to display the preprint in perpetuity. It is made available under aCC-BY-NC-ND 4.0 International license.

and its associated dynamics of driving cell state transitions is essential for rationally tailoring sequential treatment regimen to an individual patient. This perspective, borne from these findings, complements prior and current efforts that aim to create frameworks that quantify the hierarchical and multi-state switching that underlie intratumoral heterogeneity in GBM using methods such as Markov chain models or exploratory adaptation models (*78*, *79*). While these approaches define *what* states are present and the probability of transitioning from one state to another, our approach provides mechanistic insights into *how* GSCs are able to navigate the phenotypic landscape (Fig. 7E).

The repurposed use of statins in cancer treatment continues to be an active area of research (*80*). There is compelling evidence from pre-clinical models for anti-proliferative effects of pitavastatin against multiple cancers, including GBM (*81*). From a clinical perspective, evidence remains inconclusive as to whether pitavastatin does or does not have a positive effect on patients. A clinical trial to evaluate the benefit of statin use in GBM patients (NCT02029573) did not meet its primary endpoint of progression free survival at 6 months (*82*). However, it should be noted that this clinical trial evaluated the use of atorvastatin, not pitavastatin. Regardless, authors of NCT02029573 reported that high LDL cholesterol level was an important predictor of poor cancer outcomes. Along similar lines, meta-analysis of five clinical trials revealed that a subset of patients who used pitavastatin prior to GBM diagnosis had higher overall survival (*83*). Our observation that pitavastatin is effective in killing GSCs of some patients appears to be consistent with this finding. Thus, findings from prior studies and evidence presented in this work both suggest that future clinical trials on statins should recruit specific subsets of GBM patients, who have higher likelihood of benefitting from this drug.

Further, our study has uncovered mechanisms of treatment responses of PD-GSCs with varied susceptibility to pitavastatin, and leveraged that understanding to rationally potentiate drug action with secondary interventions with siRNAs or other drugs. In so doing, these findings contribute valuable foundational insights into system wide effects of pitavastatin action on PD-GSCs, with actionable strategies to minimizing treatment escape with sequentially administered secondary interventions against transcriptional regulatory mechanisms driving cell state transitions. We also demonstrate that our findings of increased efficacy of pitavastatin in combinatorial treatments with vinflunine was generalizable across PD-GSCs, especially those that were sensitive to pitavastatin. Thus, our study serves as proof-of-concept for a generalizable systems biology

bioRxiv preprint doi: https://doi.org/10.1101/2024.02.02.578510; this version posted February 7, 2024. The copyright holder for this preprint (which was not certified by peer review) is the author/funder, who has granted bioRxiv a license to display the preprint in perpetuity. It is made available under aCC-BY-NC-ND 4.0 International license.

approach that can be applied to characterize and block mechanisms of treatment escape of all cancers with rationally designed combination treatments.

Broadly speaking, our findings provide a mechanistic framework for connecting two aspects of phenotypic plasticity of tumor cells, one that characterizes discrete states (*36*), and the second that characterizes cell state continuums, including gradients defined by a neuronal developmental–injury response axis (*84*) or a PN–MES axis (*11*, *85*). Such a framework, like the seminal GBM molecular subtype classification scheme (*2*), will enable integration of the genomic, transcriptomic, and epigenomic landscapes and associated factors that underlie phenotypic plasticity of GSCs and differentiated tumor cells that define intra- and inter-tumoral heterogeneity in GBM (*2*, *4*, *36*, *86*). Ultimately, a systems approach that connects intrinsic regulatory mechanisms with extrinsic factors, including drug treatment, tumor microenvironment (*75*), and the immune response (*87*), governing phenotypic plasticity of GSCs in an individual patient's cancer, will be needed for formulating treatment strategies to prevent recurrence of drug-resistant GBM tumors.

METHODS

Ethics Statement. Use of human tissue was reviewed and approved by the WIRB-Copernicus Group Institutional Review Board (WCG® IRB). All participants provided written informed consent according to IRB guidelines prior to participation in the study. Only tissue specimens deemed non-essential for diagnostic purposes and that would otherwise be discarded were collected for research purposes.

Patient samples and patient-derived GBM stem-like cell enrichment

Tumors were obtained from surgeries performed at Swedish Medical Center (Seattle, WA) according to institutional guidelines. Patient samples used in this study were diagnosed as WHO grade IV glioblastoma. GSC cultures were established from freshly resected tumor tissues. Tissue samples were minced into 1mm^3 fragments and digested with Accutase (Sigma) at 37°C for 15-20 minutes. Neurobasal-A medium (NBM) was added to quench Accutase activity and cell suspensions were filtered through 70µm nylon mesh, centrifuged at 1K rpm for 5 min, resuspended in fresh NBM, and cultured in T75 flasks pre-treated with a laminin solution (1:100 Sigma), which includes incubation of the flasks with the laminin solution at 37°C for a minimum of 30 minutes. PD-GSCs were maintained in NBM with B-27 serum-free supplement, 20 ng/mL EGF,

bioRxiv preprint doi: https://doi.org/10.1101/2024.02.02.578510; this version posted February 7, 2024. The copyright holder for this preprint (which was not certified by peer review) is the author/funder, who has granted bioRxiv a license to display the preprint in perpetuity. It is made available under aCC-BY-NC-ND 4.0 International license.

20 ng/mL FGF-2, 20 ng/mL insulin, 1 mM sodium pyruvate, 2 mM L-glutamine and 1% Antibiotic-Antimycotic.

PD-GSC in vitro cultures

PD-GSC adherent monolayer cultures were used for all pitavastatin and pitavastatin/vinflunine treatments. Monolayer cultures were maintained in T75 flasks (cell expansion), T25 flasks (pitavastatin-treatment), or 96 well plates (IC_{50} studies) pre-treated with a laminin solution (1:100; Sigma) and incubated at 37°C for a minimum of 30 min. Serum-free culture media consisted of Neurobasal Medium-A (Gibco™) with 2.0% (v/v) B-27 serum-free supplement minus vitamin A (Gibco™), 20 ng/mL EGF (PeproTech Inc.), 20 ng/mL FGF-2 (PeproTech Inc.), 20 ng/mL insulin (Sigma), 1 mM sodium pyruvate (Corning), 2 mM L-glutamine (Gibco™) and 1% Antibiotic-Antimycotic (Gibco™). PD-GSC monolayer cultures were maintained at 37°C, 5% CO2 atmospheric oxygen with culture pH monitored with the phenol red. Cultures were refed every 2-3 days. PD-GSC cultures tested were within 10 passages from the initial GSC enrichment from the original tumor biopsy.

PD-GSCs were passaged by dissociating monolayer cultures from the respective substrate by treating the cells with the dissociation reagent Accutase (1mL/25cm^2) or TrypLE™ (1mL/25cm^2 – see *Flow cytometry CD44 and CD133 analysis* section) at 37°C for 5min. Pre-warmed (37°C) serum-free culture media (described above) was then added to quench dissociation reagent activity (1:3 media:dissociation reagent ratio). The resulting cell suspension was centrifuged at 1K rpm (193g) for five minutes. The cell pellet was resuspended in fresh serum-free culture media, and added to QS serum-free culture media in a new laminin-treated flask. Final culture volumes were as follows: T75 – 10mL, T25 – 5mL, 96-well plate – 100μL. Laminin treatment involved incubating flasks (or 96 well plates) with a laminin working solution (5mL/75cm^2), which consisted of stock laminin (Sigma) diluted 1:100 in phosphate buffer solution, at 37°C for a minimum of 30 min.

Flow cytometry – apoptosis, caspase 3/7-mediated apoptosis, and cell-death

Data acquisition of surface protein markers was performed on the Attune NxT Flow Cytometer (ThermoFisher Scientific). PD-GSCs were dissociated from their respective substrate using Accutase and washed twice with PBS + FBS serum (10%), which involved centrifugation at 1K rpm (193g) for 5 min, supernatant removal, and cell pellet resuspension with the PBS + FBS serum (10%). The supernatant wash was removed and the cell pellet resuspended in the

bioRxiv preprint doi: https://doi.org/10.1101/2024.02.02.578510; this version posted February 7, 2024. The copyright holder for this preprint (which was not certified by peer review) is the author/funder, who has granted bioRxiv a license to display the preprint in perpetuity. It is made available under aCC-BY-NC-ND 4.0 International license.

PBS/FBS solution to the desired concentration of 1e6 cells/mL. To assess apoptosis, caspase 3/7-mediated apoptosis, and cell death within the GSC populations, cells were stained with Annexin V conjugated with Alexa Fluro 568 (Invitrogen A13202), CellEvent™ Caspase 3/7 detection reagent (Invitrogen C10423), and SYTOX™ AAdvanced Dead Cell Stain (Invitrogen S10349), simultaneously. Samples were stained following each of the manufacturer's protocol, respectively. Gating for positive and negative expressing cells was performed using FlowJo V10 based on multiple controls including, 1) unstained negative controls, 2) heat-inactivated cells (incubated in a 60°C water bath for 15 min), which served as positive controls for apoptotic and dead cells, and 3) Fluorescence minus one (FMO) controls to define an upper boundary for background signal on the omitted signal and gate for positively stained populations in multi-color experiments.

Flow cytometry – CD44 and CD133 analysis

Samples from each treatment condition were collected using TrypLE™ (Gibco™) to dissociate and remove the cells from the culture flasks. TrypLE™ (1mL/25cm^2) was used to minimize any structural changes on CD44 and CD133 surface proteins during the dissociation process (*88*). Subsequent sample processing prior to antibody staining was identical to how samples were processed for apoptosis, caspase 3/7-mediated apoptosis, and cell-death cytometry assessment. An anti-Hu CD44 antibody conjugated with PE (eBiosciences™) and an anti-Hu/Mo CD133 antibody conjugated with FITC (eBiosciences™) were used to assess expression of these two surface proteins across each PD-GSC population. Samples were simultaneously treated with both antibodies per vendors' recommendations. Analysis of flow cytometry data was performed using FlowJo V10. Fluorescent signal gating was set based on multiple control samples including: 1) unstained PD-GSC negative controls, 2) vendor-recommended isotype controls (Mouse IgG1 kappa isotype and Rat IgG2b kappa isotype for anti-Hu CD133 and anti-Hu/Mo CD44, respectively, 3) human GBM stem cells (Cellprogen Inc.), which served as a positive control cell line for both CD133 and CD44 (per vendor's specification), and 3) Caco2 cells, (ATCC) which served as a positive control cells for CD133 and negative controls for CD44.

Pitavastatin treatment of PD-GSCs for scRNA-seq and flow cytometry analysis

PD-GSCs were incubated in serum-free culture media (described above) with pitavastatin (6μM). Stock pitvastatin calcium (Selleck Chemicals LLC) was dissolved in DMSO to obtain a stock concentration of 10mg/mL and stored in aliquots at -80°C. Stock pitavastatin calcium solution was

bioRxiv preprint doi: https://doi.org/10.1101/2024.02.02.578510; this version posted February 7, 2024. The copyright holder for this preprint (which was not certified by peer review) is the author/funder, who has granted bioRxiv a license to display the preprint in perpetuity. It is made available under aCC-BY-NC-ND 4.0 International license.

serially diluted in serum-free culture media to 100μM and then to the final concentration of 6μM with a final DMSO concentration of 0.053% (v/v).

To monitor longitudinally PD-GSC response to pitavastatin, we performed a reverse time-course treatment by adding pitavastatin to SN520 and SN503 cultures in a staggered fashion such that the longest (4-day) treatment would have drug added first. Subsequent addition of pitavastatin would occur on following days for 3- and 2-day treatment, respectively. This reverse time course design allowed us to collect all samples simultaneously on day four following the initial addition of pitavastatin. Because pitavastatin was added to PD-GSCs on different days, flasks were inoculated at slightly different cell densities to account for cell growth that would occur in between inoculation and time of pitavastatin addition. Consequently, scRNA-seq library preparation of all samples for a particular PD-GSC population occurred simultaneously to minimize batch effects due to individual sample processing (table S16)

Prior to T25 flask (BioLite^{TM}) inoculation for pitavastatin treatment, PD-GSCs were first expanded in a T75 flask (BioLite^{TM}). Once the culture was confluent, the culture was harvested and split into laminin-treated T25 flasks. Upon inoculation, cells were incubated in serum-free culture media at 37°C for 24 hours to allow cells to adhere to the interior surface of the flask. Following the first 24 hours, serum-free culture media was replaced with serum-free culture media with pitavastatin (6μM) in T25 flasks predetermined to receive a 4-day treatment. Spent culture media would then be replaced with fresh culture media with pitavastatin (6μM) on subsequent days for D3 and D2 treatment conditions.

Upon the completion of the 4-day treatment, spent media was removed and cells were harvested using Accutase^{TM} (1mL/25cm^2). To prevent any cell-free DNA/RNA from treatment-induced lysed cells contaminating single-cell samples, we first processed a portion of the cell harvest solution using the dead cell removal kit (Miltenyi Biotec 130-090-101) to remove any cell debris to avoid any free RNA from lysed cells from getting mixed in with mRNA to be extracted from live cells. Samples were processed per vendor's specifications. The result was a cell suspension of the remaining live cells post vehicle- or pitavastatin-treatment. Cell suspension was then processed for scRNA-seq profiling per the 10X Chromium platform.

scRNA-seq library prep and sequencing

bioRxiv preprint doi: https://doi.org/10.1101/2024.02.02.578510; this version posted February 7, 2024. The copyright holder for this preprint (which was not certified by peer review) is the author/funder, who has granted bioRxiv a license to display the preprint in perpetuity. It is made available under aCC-BY-NC-ND 4.0 International license.

Single-cell RNA sequencing was performed using the 10X Chromium v2 system. Library preparation was performed using 10x manufacturer instructions on an Illumina NovaSeq 6000. scATAC-seq was performed as per manufacturer instructions (Single-cell ATAC Reagent Kits v1.1 UserGuide RevD) and sequenced on an Illumina NextSeq 500.

Multi-passage, pitavastatin treatment

PD-GSCs were harvested from a T75 flask and passaged into replicate T75 flasks for either pitavastatin (6μM) or vehicle (DMSO) treatment (2.0e6 cells/flask). Concomitantly, a portion of those PD-GSCs were used to inoculate laminin-treated 96 well plates for drug-dosing analysis (see *IC_{50} Analysis* section). On D4, PD-GSCs were harvested using Accutase (1mL/25cm^2) as described previously. Cell suspensions were spun at 1000rpm (193g) for five minutes. Cell pellets were then resuspended with serum-free culture media (200,000 cells/mL) to inoculate 96 well plates (100μL/well, 20,000 cells/well) for subsequent IC_{50} determination. PD-GSCs were incubated in serum-free culture media in 96 well plates for 48 hours to allow for cell attachment prior to replacing spent media with serum-free media with pitavastatin (or vehicle). Treated cells were incubated at 37°C for four days. Following the four-day treatment, cell viability was measured via MTT assay as described below.

DNA quantification via propidium iodide (PI) staining

PD-GSC cultures were treated with pitavastatin (or vehicle control) in a reverse time-course manner as described previously (*Pitavastatin treatment of PD-GSCs for scRNA-seq and flow cytometry analysis* section). Following cell harvest, PD-GSCs were washed with PBS and spun down at 1000 RPMs (193 g) for 5 minutes. PD-GSCs were then fixed with cold 70% ethanol by adding 70% ethanol drop-wise to the pellet while vortexing. Cells were fixed in 70% ethanol overnight at 4°C. Once fixation was complete, the PD-GSCs were washed twice in PBS, spun down at 1000 rpms for five minutes with careful removal of the supernatant so as to avoid any cell loss. PD-GSCs were then treated with 50μL of ribonuclease (100μg/mL stock) to remove any RNA and ensure only DNA would be stained. Finally, 200μL of propidium iodide (PI, 50μg/mL stock) was added to the fixed and treated cells prior to flow cytometry analysis.

IC_{50} Analysis and MTT viability assay

3-(4,5-Dimethyl-2-thiazolyl)-2,5-diphenyl-2H-tetrazolium bromide, (MTT) assay was used to determine the effects of pitavastatin on the viability of the non-responsive and responsive GSC populations. Briefly, 20,000 cells/well were plated in laminin-treated 96-well plates with 100uL of

bioRxiv preprint doi: https://doi.org/10.1101/2024.02.02.578510; this version posted February 7, 2024. The copyright holder for this preprint (which was not certified by peer review) is the author/funder, who has granted bioRxiv a license to display the preprint in perpetuity. It is made available under aCC-BY-NC-ND 4.0 International license.

culture media. Following an initial 24hr incubation, the cells were treated with 100μL of culture media with pitavastatin at varying concentrations (0.0, 0.1, 0.6, 1.0, 3.0, 6.0, 10.0, 33.0μM) and incubated at 37C for four days. Vehicle amounts were adjusted such that the vehicle concentration in all conditions was equivalent to the maximum drug dosage tested (DMSO 0.2% v/v). Following the 4-day treatment, spent media was replaced with 100μL of serum-free culture media with MTT (0.5mg/mL) and incubated at 37°C for 60 minutes. Following incubation, supernatant from each well was discarded and replaced with 100μL of DMSO to dissolve the formazan crystals formed during MTT incubation. Absorbance (A_i, where i is the drug concentration) was measured via spectrophotometer at 570nm (Synergy H4, Agilent Technologies, Inc.). Relative viability was calculated using the following formula: relative viability = $(A_i - A_{background})/A_{0.0} * 100\%$, where $A_{background}$ is the absorbance from DMSO. IC_{50} values were calculated by using a 4-parameter log-logistic model determined by the *drm()* function within the *drc* package in R. Here, the upper limit of the log-logistic model was set to 100%.

siRNA treatment

Following a 24hr incubation period, cells were treated with 5μM of Accell SMARTpool siRNA or Accell SMARTpool Non-Targeting siRNA (Dharmacon Inc.). Lyophilized SMARTpool siRNAs were resuspended in 1X siRNA buffer (Dharmacon Inc.) and subsequently diluted in serum-free culture media to a final concentration of 5μM. Based on vendor recommendations, Accell siRNA designs facilitate siRNA delivery to the target cell and do not require additional transfection reagents. Accell SMARTpool siRNAs pools consist of four separate siRNAs designed to target a particular gene. To test the efficacy of *sequential* treatment of pitavastatin followed by siRNA-mediated knockdown of specific TFs, pitavastatin (1.0μM or 6.0μM for SN520 and SN503, respectively) and siRNA (5μM) were added simultaneously followed by a four-day incubation at 37°C due to the delayed effect in which siRNAs would be maximally effective in the cells, per vendor recommendations. To test the simultaneous effect of pitavastatin and siRNA-mediated knockdown, siRNA was added to PD-GSC cultures 24hrs post cell inoculation and allowed to incubate for 2 days. Pitavastatin was then added to cultures such that the final concentration reached 1.0μM or 6.0μM for SN520 and SN503, respectively. Relative viabilities with respect to non-template controls were calculated by first normalizing a relative viability values with respect to siRNA and drug-free condition (pitavastatin = 0.0μM) and then normalizing that with respect to the NTC condition. All siRNA tests were performed in laminin-treated 96 well plates with an inoculation density of 20,000 cells/well and a final volume of 100uL of culture media/drugs/siRNA.

bioRxiv preprint doi: https://doi.org/10.1101/2024.02.02.578510; this version posted February 7, 2024. The copyright holder for this preprint (which was not certified by peer review) is the author/funder, who has granted bioRxiv a license to display the preprint in perpetuity. It is made available under aCC-BY-NC-ND 4.0 International license.

Bulk RNA-seq library prep and sequencing

Total RNA was extracted from PD-GSC cultures using mirVANA™ miRNA isolation kit (ThermoFisher). Residual DNA was removed using the RQI RNAse-Free DNase kit (Promega). Total RNA was then quantified using the Agilent RNA 6000 nano kit (catalogue number) on the Agilent 2100 BioAnalyzer. 1μg of of high purity RNA was used as input to the Illumina TrueSeq Stranded mRNA Library Prep Kit and sample libraries were generated per manufacturer's specifications. The RNA-seq libraries were sequenced on the NextSeq 500 next gen sequencer using a paired end high-output 150bp v2.5 flowcell. Sequence intensity files were generated on instrument using the Illumina Real Time Analysis software. The resulting intensity files were de-multiplexed with the bcl2fastq2 software.

Processing and normalization of bulk RNA-seq data

Raw RNA-seq data of samples encoded in FASTQ-files were subjected to a standardized RNA-seq alignment pipeline. In summary, RNA-seq reads were trimmed and clipped of Illumina sequence adapters via Trim Galore (https://github.com/FelixKrueger/TrimGalore), mapped to human reference genome (GRCh38) using STAR (v2.7.3a), and counted using HTSeq (v 0.11.1). Individual sample counts were combined into a single data object using the *DESeqDataSetFromHTSeqCoun*t function in DESeq2 (*89*). Sample-specific size factors were determined and used to normalize counts, which were transformed using regularized log transformation for subsequent downstream analysis, performed in R.

scRNA-seq data QC filtering and normalization

We initially processed the 10X Genomics raw data using Cell Ranger Single-Cell Software Suite (release 3.1.0) to perform alignment, filtering, barcode counting, and UMI counting. Reads were aligned to the GRCh38 reference genome using the pre-built annotation package download from the 10X Genomics website. We then aggregated the outputs from different lanes using the *cellrange aggr* function with default parameter settings.

SN520 and SN503 scRNA-seq data sets were QC-filtered separately prior subsequent downstream analysis. To minimize inclusion of poor-quality genes and single-cell samples per sample set, we applied the following QC filters: 1) mitochondrial genes must comprise ≤ 6.5% of the number of uniquely mapped genes/cell, and 2) total counts/cell should be ≥ 7500 and ≤ 60,000. Post QC-filtering, each scRNA-seq data set included: 5,402 cells expressing up to 18,227

bioRxiv preprint doi: https://doi.org/10.1101/2024.02.02.578510; this version posted February 7, 2024. The copyright holder for this preprint (which was not certified by peer review) is the author/funder, who has granted bioRxiv a license to display the preprint in perpetuity. It is made available under aCC-BY-NC-ND 4.0 International license.

884 genes (SN520) and 5,722 cells expressing up to 18,797 genes (SN503). Subsequent
885 normalization and downstream analysis (e.g., DEG and functional enrichment analysis) was
886 performed using the Seurat v3.2.2 platform (*90*).
887
888 Normalization was performed for each scRNA-seq dataset separately by computing pool-based
889 size factors that were subsequently deconvolved to obtain cell-based size factors using the
890 *computeSumFactors* function within the *scran* package (version 1.10.2) (*91*) in R. Normalized log
891 expression values were used for subsequent downstream analysis.
892
893 **Batch integration of scRNA-seq data**
894 As each PD-GSC-specific data set was collected separately, we performed batch correction on
895 the scRNA-seq data to integrate the SN520 and SN503 data sets by applying the Harmony
896 algorithm (*33*). Subsequent SNN-graph formation and UMAP embedding was performed on the
897 Harmony-corrected PCs (Fig. 1E).
898
899 **Cell-cycle analysis**
900 To annotate individual cells with their respective cell cycle phase, we performed cell cycle analysis
901 using the Seurat program. Briefly, core sets of 43 and 54 genes associated with the S- and G2/M-
902 phases, included in the Seurat platform, were used to determine a cell-cycle phase score based
903 on the expression of the respective markers. Based on these scores, cells were assigned to be
904 either in G1 or G2/M phase. Cells not expressing genes from either set were considered as not
905 cycling and assigned to the G1 phase. Using these quantitative scores, we also regressed out
906 cell-cycle effects on expression for each cell using the *ScaleData* function in Seurat as part of the
907 pre-processing steps to QC the scRNA-seq data.
908
909 **Cluster identification and analysis of differentially expressed genes (DEGs).**
910 After quality control and filtering the scran-normalized scRNA-seq data, we performed
911 dimensionality reduction via principal component analysis (PCA). The first 30 principal
912 components were used as a basis to create a shared nearest neighbor (SNN) graph of the single-
913 cell samples. From this graph, clusters of single cells were identified via Louvain clustering of
914 nodes, i.e., single cells, from the SNN graph.
915
916 To identify DEGs in each of the SNN-clusters identified across the primary tumor and PDX single-
917 cell samples, the *FindMarkers* function in Seurat was used. In particular, the Wilcoxon rank sum

bioRxiv preprint doi: https://doi.org/10.1101/2024.02.02.578510; this version posted February 7, 2024. The copyright holder for this preprint (which was not certified by peer review) is the author/funder, who has granted bioRxiv a license to display the preprint in perpetuity. It is made available under aCC-BY-NC-ND 4.0 International license.

test was used with the following cutoff values to identify DEGs: absolute log-fold change ≥ log2(1.5), with a minimum proportion of 10% of the cells of interest expressing the gene of interest, and an FDR-adjusted p-value ≤ 0.1.

Gene set variance analysis (GSVA) enrichment scores and statistical significance

Gene set variance analysis GSVA (version 1.34.0, R package) (*32*) was used to determine enrichment scores of GBM molecular subtypes. To define the dominant molecular subtype gene expression signature in each single cell, we used an amalgamation of the original gene sets that defined the classical, proneural, and mesenchymal subtypes (*2*) and refined molecular subtype gene sets (*3*) for GSVA.

Critical Transition Index (I_c)

A brief explanation of I_c from (*55*) is reproduced for reference. The critical transition index is a scalar value that quantifies if a cell is undergoing (high Ic) or has undergone some critical transition and reached some stable cell state (low Ic). I_c is calculated according to the following:

$$I_c(t) = \frac{\langle |R(g_i, g_j)| \rangle}{\langle R(S^k, S^l) \rangle} \quad (1)$$

Where R is Pearson's correlation coefficient between two observed cell state vectors S^k and S^l or between two "gene" vectors g_i and g_j, respectively, taken from the gene expression data matrix representing the state(s) of a "cell ensemble" $X(t)$

$$X(t) = \begin{bmatrix} x_1^1 & \cdots & x_m^1 \\ \vdots & \ddots & \vdots \\ x_1^n & \cdots & x_m^n \end{bmatrix} \quad (2)$$

$X(t)$ thus represents the data of a "measurement point", with access to finer-grained layer of information given the single-cell nature of the data. Each row represents a single-cell in some state k within the cell-ensemble of n-cells in m-dimensional gene state space – $S^k = [x_1^k, x_2^k, \ldots, x_m^k]$. Each column represents gene i's expression across n cells from said "cell ensemble" $X(t)$, where $g_i = [x_i^1, x_i^2, \ldots, x_i^n]$. The brackets $\langle \cdots \rangle$ in equation 1 represent the average of all correlation coefficients R between all pairs of state vectors S or gene vectors g from matrix

bioRxiv preprint doi: https://doi.org/10.1101/2024.02.02.578510; this version posted February 7, 2024. The copyright holder for this preprint (which was not certified by peer review) is the author/funder, who has granted bioRxiv a license to display the preprint in perpetuity. It is made available under aCC-BY-NC-ND 4.0 International license.

946 $X(t)$. Here, a cell-ensemble represented the population of PD-GSCs at a particular treatment time-
947 point (D0, D2, D3, or D4).
948
949 The underlying premise is that cells that have undergone some critical transition into an attractor
950 state will be nominally expressing the same distinct gene expression pattern, with the exception
951 of deviations due to stochastic fluctuations. Consequently, cells of the same differentiated state
952 will be expressing similar gene expression programs and will correlate highly with one another.
953 Characteristic gene expression of cells within a particular attractor state is affected by symmetric
954 random fluctuations. Thus, gene-to-gene coupling is dominated by noise, reducing gene-to-gene
955 correlations. Conversely, destabilized cells undergoing some transition, requires some non-
956 random shift in gene expression patterns that override the symmetric noise expected in cells
957 within a stable attractor state.
958
959 **MINER network inference**
960 An additional gene-filtering step was performed on the QC scRNA-seq data sets to identify a
961 common gene set between SN520 and SN503 – only common genes having a minimum gene
962 count ≥ 2 in a minimum of 20 cells were considered for network inference. This resulted in a
963 common gene set of 9,089 common genes used in SN520 and SN503 for MINER3 network
964 inference.
965
966 To infer regulons within single cells, we applied the MINER (*46*) workflow to the SN520 and SN503
967 scRNA-seq data sets independently. As part of the scSYGNAL framework, the MINER algorithm
968 involves a suite of functions that enables the inference of causal mechanistic relationships linking
969 genetic mutations to transcriptional regulation. Because our datasets did not include any
970 mutational profiling, we primarily focused on identifying regulons, based on co-expression
971 clustering and enrichment of transcription factor binding motifs present in those co-expression
972 clusters identified, and calculated the activity of these regulons in the single-cell samples. Broadly
973 speaking, regulon activity represents the “eigengene” value in an individual cell. Regulons are
974 identified, in part, by performing PCA on the normalized scRNA-seq data profiles to identify
975 principal components in which decreasing amounts of variation across genes are captured along
976 each principal component – defined as a linear combination of gene expression values. This linear
977 combination of weighted gene expression values defines the eigengene value per sample (*43*,
978 *44*, *46*, *92*). Alternatively, the eigengene is defined as the first principal component of the module

bioRxiv preprint doi: https://doi.org/10.1101/2024.02.02.578510; this version posted February 7, 2024. The copyright holder for this preprint (which was not certified by peer review) is the author/funder, who has granted bioRxiv a license to display the preprint in perpetuity. It is made available under aCC-BY-NC-ND 4.0 International license.

expression matrix composed of expression values of regulon genes across samples. It is a scalar representation of expression of gene members for a regulon in an individual sample (*92*).

To determine the significance of each inferred regulon, we performed a permutation test to determine the possibility of obtaining an eigenvalue corresponding to the first principal component of a regulon (across all single-cells) of equal or greater value. The eigenvalue represents a summarizing value of all the genes in the regulon, i.e., eigengene and thus if these genes are indeed coregulated or are correlated, the eigengene value would be higher than that of randomly selected set of genes. Next, we randomly select a set of genes having the same number of members as the original regulon and calculate the corresponding eigengene value for the permuted regulon. This procedure was repeated 1,000 times to create a null distribution of eigengene values. We repeated this procedure for each inferred regulon. Those regulons whose eigengene values were greater than the 95th percentile of their respective null distribution were considered significant. These eigengene values represented regulon "activity" within each cell. We further filtered out regulons in which the first principal component from the module expression matrix composed of expression values of regulon genes across samples did not account for at least 20% of the variation of the module expression matrix. From these two criteria, statistical significance of an eigengene and variance explained within the module expression matrix were used to refine the number of regulons to include for SN520 and SN503, respectively.

Pseudotime/latent time analysis

We applied Monocle v3 in R (*93*, *94*) and scVelo (*54*) to organize cells along pseudotime axes and identify distinct trajectories along which transcriptomic expression states putatively transition. Scran-normalized scRNA-seq datasets were used to infer pseudotime trajectories for SN520 and SN503 independently using the *learn_graph* and *order_cells* function in Monocle v3 (v1.2.7) and default parameter settings.

In parallel, we analyzed transcriptional dynamics by determining latent time using scVelo (*54*). Transcriptome dynamics were inferred using the *latent_time* function and default parameter settings.

Locally estimated scatterplot smoothing (LOESS) regression analysis

We performed LOESS regression on individual TF expression across the single cells along the inferred pseudotime trajectories. This allowed us to fit a polynomial regression line through the

bioRxiv preprint doi: https://doi.org/10.1101/2024.02.02.578510; this version posted February 7, 2024. The copyright holder for this preprint (which was not certified by peer review) is the author/funder, who has granted bioRxiv a license to display the preprint in perpetuity. It is made available under aCC-BY-NC-ND 4.0 International license.

highly variable single-cell gene expression to identify any underlying patterns that may be present over pseudotime. LOESS regression of normalized single-cell gene expression along pseudotime was performed using the *loess* function within the *stats v3.6.2* package in R.

TF-TF network topology inference

To generate TF-TF network topologies, we cross-referenced all regulator-target gene connections inferred by MINER3 against the transcription factor binding site database (tfbsdb.systemsbiology.net), focusing on only those interactions that involved pairs of TFs that were also regulators for some regulon. The type of TF-TF interaction was determined by the sign of the pairwise Pearson correlation between the two components – positive correlations were interpreted as activating interactions while negative correlations were interpreted as inhibiting interactions. We further refined the TF-TF network by removing those interactions having an absolute Pearson correlation coefficient (r) below a statistically significant minimum threshold, determined by permutation analysis ($|r| \geq 0.17$ for SN520 and $|r| \geq 0.16$ from SN503). Permutation tests involved randomly mixing expression values across genes within a single-cell and calculating Pearson's r among all gene pairs across all PD-GSCs for SN520 and SN503 independently. This process was repeated 1000 times to create a null distribution of Pearson correlation coefficients.

To determine the statistical significance of each network TF-TF network topology, we performed two sets of permutation tests. Briefly, the first set of permutation tests involved permuting the network topology, where node labels and edges were permuted such that the number of edges and nodes remained consistent, we performed dynamic simulation for the permuted network using initial condition, i.e., TF expression profiles from a randomly selected untreated (D0) cell for each PD-GSC, respectively. The simulated results were then compared to experimental data to determine cosine similarity values. This permutation-simulation-comparison process was repeated 1,000 times to create a null distribution of cosine similarity values. The distribution of cosine similarity values derived from the original TF-TF network topologies were significantly higher than the permuted similarity values (fig. S12). The second set of permutations involved permuting the gene expression data, mixing the gene and cell ids to see if similar TF-expression states could be achieved by random chance. Cell and gene labels were permuted 1000 times to create a permuted distribution of TF-expression states, which were then compared to the original experimental states, defined by hierarchical clustering, using pairwise cosine similarity values (fig. S12).

bioRxiv preprint doi: https://doi.org/10.1101/2024.02.02.578510; this version posted February 7, 2024. The copyright holder for this preprint (which was not certified by peer review) is the author/funder, who has granted bioRxiv a license to display the preprint in perpetuity. It is made available under aCC-BY-NC-ND 4.0 International license.

RACIPE simulations

Simulations were performed using the sRACIPE package v1.16.0 in R. Briefly, using sRACIPE we generated an ensemble of ordinary differential equation (ODE) models based on associated chemical rate equations with distinct, randomly generated kinetic parameter sets. From the ensemble of models, we analyze the resulting distribution of steady states and identify robust phenotypes supported by the core TF network. The inferred TF-TF network topology for SN520 (or SN503) was used as the input circuit for the *sracipeSimulate* function. An integral step size of 0.2 and simulation time of 100 was used for simulations.

To verify the ability of the network topology to recapitulate observed TF expression states, we initialized the network by randomly selecting 1,000 expression profiles (with replacement) for the respective TFs from D0 scRNA-seq profiles for each PD-GSC, i.e., initial conditions that were paired with 1,000 parameter models randomly selected by the *sracipeSimulate* function (default settings used).

To explore the plausible network states supported by each network topology, we initialized each network topology by using 100 randomly selected initial conditions that were used across 10,000 randomly selected parameter sets, which resulted in an ensemble of 1 million simulated steady-states. To determine the dominant steady states from the ensemble of simulations, all Euclidean pairwise distances were calculated. Those simulated states that had a Euclidean pairwise distance $\geq$ 4.0 (scSYGNAL-520) or $\geq$ 1.92 (scSYGNAL-503) were labeled as a “non-redundant” state. The distance thresholds were found to be the $\geq 99^{th}$ percentile of permuted Euclidean pairwise distances for each PD-GSC, which was determined by randomly selecting 1,000 pairs of simulated states and calculating all pairwise Euclidean distances. This process was repeated 10 times to create a distribution of 10 million pairwise Euclidean distances. From these distance thresholds, we identified 6,519 (scSYGNAL-520) and 4,223 (scSYGNAL-503) simulated states were deemed as unique states. We then hierarchically clustered each set of distinct, “non-redundant” states and identified four dominant states that were supported by each TF-TF network topology (Fig. 6C, E). To classify a “redundant” simulated state, we assigned it the same state as its nearest “non-redundant” neighbor, based on Euclidean distance.

RACIPE convergence tests

bioRxiv preprint doi: https://doi.org/10.1101/2024.02.02.578510; this version posted February 7, 2024. The copyright holder for this preprint (which was not certified by peer review) is the author/funder, who has granted bioRxiv a license to display the preprint in perpetuity. It is made available under aCC-BY-NC-ND 4.0 International license.

To verify that the number of initial conditions and parameter sets would sufficiently converge to steady state solutions across the initial condition and parameter space, we performed a series of simulations using 100 randomly selected initial conditions across different number of model parameters (1e3, 2e3, 4e3, 6e3, 8e3, and 1e4). The result was a series of simulations consisting of six different ensembles of simulated states, one for each model parameter set, with each ensemble associated with a randomly selected set of initial conditions. This series of simulations was performed in triplicate. For each set of results, we identified the unique states using the same Euclidean distance thresholds described in *RACIPE simulations*. Next, we determined the Kullback-Liebler (KL) divergence for these simulated states across the triplicate set of simulations for each set of results (fig. S13).

Random Forest analysis of RACIPE simulations

Random forest analysis was performed on RACIPE simulations, i.e., simulated transcriptional states for SN520 and SN503 using *randomForest* function (default parameters) from the *randomForest* package v4.7-1.1. Simulated state classifiers were based on hierarchical clustering of the unique (non-redundant) simulated states as described in *RACIPE simulations*.

Drug Matching Identification

To identify drugs targeting elements within the transcriptional programs identified from the network analysis, we applied the Open Targets platform tool (https://www.targetvalidation.org/). The platform integrates a variety of data and evidence from genetics, genomics, transcriptomics, drug, animal models, and literature to score and rank target-disease associations for drug target identification. We focused our search on identifying drug-target matches for only those drugs associated with any cancer treatments that had reached Phase IV matching with regulon genes associated with SN520. Originally, 28 drugs paired with genes across 17 regulons. We further refined the list of potential drug candidates to those drugs associated with GBM, reducing the number of candidate drugs to eight, including vinflunine.

ACKNOWLEDGEMENTS

We thank M. Strasser for insightful discussions and advice on simulating and analyzing TF-TF network dynamics; M. Arietta-Ortiz for advice on TF-TF network analysis and testing; H. Hampton on advice on experimental design and analysis of flow cytometry data; A. Akade for helpful discussion on stem-cell culture methodologies; C. Lausted for advice on experimental design for

bioRxiv preprint doi: https://doi.org/10.1101/2024.02.02.578510; this version posted February 7, 2024. The copyright holder for this preprint (which was not certified by peer review) is the author/funder, who has granted bioRxiv a license to display the preprint in perpetuity. It is made available under aCC-BY-NC-ND 4.0 International license.

single-cell RNA-seq; and the entire Baliga laboratory for general support and advice. We would also like to thank the ISB Molecular Core for their services in preparing and sequencing the single-cell samples and Timothy J. Martins and the University of Washington Quellos High-throughput Screening Core for advice and services in running HTP screens. JP was funded by a fellowship from the NIH (F32-CA247445) and currently supported by NIH grant R01-CA259469. PH was funded by the Ben and Catherin Ivy Foundation and is currently supported by R01-CA259469 and philanthropic funding from Swedish Medical Center Foundation. AL was supported by R01-AI141953. MP is supported by R01-AI128215 and R01-CA259469, RC was supported by R01-CA259469, WW is supported by R01-AI128215 and R01-CA259469, and ST is supported by R01-AI128215 and R01-CA259469. HL is supported by R01-CA259469 and philanthropic funding from the Swedish Medical Center Foundation. APP is supported by R01-NS119650, the Burroughs Wellcome Career Award for Medical Scientists, and Discovery Grant from the Kuni Foundation. CC is supported by R01-CA259469. SH is supported by R01-GM109964, R01-CA226258, R01-GM135396, and R01-CA255536. NSB is supported by R01-AI128215, R01-CA259469, and R01-AI141953.

Author Contributions

JP, SH, and NSB conceived the study. JP designed all experiments with guidance from AL, MP, PH, CC, SH, and NSB. Pitavastatin-treatment experiments for bulk and single-cell RNA-seq, and all flow cytometry-related experiments were performed by JP. MP prepared samples for bulk RNA sequencing. JP, MP, and RC performed all siRNA-related experiments. PH and CC organized and executed the HTP drug screen. PH and HL performed sequential drug treatment experiments. JP analyzed all data and performed all network dynamics simulations with guidance from APP, SH, and NSB. WW and ST performed miRNA regulation and drug targeting analysis. JP and NSB wrote the original draft paper with input from all authors. JP, PH, SH, and NSB revised and edited the manuscript.

Competing Interests

NSB is a co-founder and member of the Board of Directors of Sygnomics, Inc., which will commercialize the SYGNAL technology. The terms of this arrangement have been reviewed and approved by ISB in accordance with its conflict of interest policy. APP is a consultant for and has an equity interest in Sygnomics, Inc. CC and PH hold a patent titled “Methods and panels of

bioRxiv preprint doi: https://doi.org/10.1101/2024.02.02.578510; this version posted February 7, 2024. The copyright holder for this preprint (which was not certified by peer review) is the author/funder, who has granted bioRxiv a license to display the preprint in perpetuity. It is made available under aCC-BY-NC-ND 4.0 International license.

compounds for characterization of glioblastoma multiforme tumors and cancer stem cells thereof" (#US11499972B2).

Data and Materials Availability

All data needed to evaluate the conclusions in the paper are present in the paper and/or Supplementary Materials. Raw single-cell sequencing data have been deposited in in NCBI database of Genotypes and Phenotypes (dbGaP) with the accession number phs003501.v1.p1.

Code for analysis of figures will be made available in Zenodo.

bioRxiv preprint doi: https://doi.org/10.1101/2024.02.02.578510; this version posted February 7, 2024. The copyright holder for this preprint (which was not certified by peer review) is the author/funder, who has granted bioRxiv a license to display the preprint in perpetuity. It is made available under aCC-BY-NC-ND 4.0 International license.

REFERENCES

1. R. Stupp, W. Mason, M. J. van den Bent, M. Weller, B. M. Fisher, M. J. B. Taphoorn, K. Belanger, A. A. Brandes, C. Marosi, U. Bogdahn, J. Curschmann, R. C. Janzer, S. K. Ludwin, T. Gorlia, A. Allgeier, D. Lacombe, G. Cairncross, E. Eisenhauer, R. O. Mirimanoff, Radiotherapy plus Concomitant\nand Adjuvant Temozolomide for Glioblastoma. *N. Engl. J. Med.* (2005), doi:10.1056/NEJMoa043330.
2. R. G. W. Verhaak, K. A. Hoadley, E. Purdom, V. Wang, Y. Qi, M. D. Wilkerson, C. R. Miller, L. Ding, T. Golub, J. P. Mesirov, G. Alexe, M. Lawrence, M. O'Kelly, P. Tamayo, B. A. Weir, S. Gabriel, W. Winckler, S. Gupta, L. Jakkula, H. S. Feiler, J. G. Hodgson, C. D. James, J. N. Sarkaria, C. Brennan, A. Kahn, P. T. Spellman, R. K. Wilson, T. P. Speed, J. W. Gray, M. Meyerson, G. Getz, C. M. Perou, D. N. Hayes, Integrated Genomic Analysis Identifies Clinically Relevant Subtypes of Glioblastoma Characterized by Abnormalities in PDGFRA, IDH1, EGFR, and NF1. *Cancer Cell*. **17**, 98–110 (2010).
3. Q. Wang, B. Hu, X. Hu, H. Kim, M. Squatrito, L. Scarpace, A. C. deCarvalho, S. Lyu, P. Li, Y. Li, F. Barthel, H. J. Cho, Y. H. Lin, N. Satani, E. Martinez-Ledesma, S. Zheng, E. Chang, C. E. G. Sauvé, A. Olar, Z. D. Lan, G. Finocchiaro, J. J. Phillips, M. S. Berger, K. R. Gabrusiewicz, G. Wang, E. Eskilsson, J. Hu, T. Mikkelsen, R. A. DePinho, F. Muller, A. B. Heimberger, E. P. Sulman, D. H. Nam, R. G. W. Verhaak, Tumor Evolution of Glioma-Intrinsic Gene Expression Subtypes Associates with Immunological Changes in the Microenvironment. *Cancer Cell*. **32**, 42-56.e6 (2017).
4. A. P. Patel, I. Tirosh, J. J. Trombetta, A. K. Shalek, S. M. Gillespie, H. Wakimoto, D. P. Cahill, B. V. Nahed, W. T. Curry, R. L. Martuza, D. N. Louis, O. Rozenblatt-Rosen, M. L. Suva, A. Regev, B. E. Bernstein, Single-cell RNA-seq highlights intratumoral heterogeneity in primary glioblastoma. *Science (80-.).* **344**, 1396–1401 (2014).
5. J. Chen, Y. Li, T.-S. Yu, R. M. McKay, D. K. Burns, S. G. Kernie, L. F. Parada, A restricted cell population propagates glioblastoma growth after chemotherapy. *Nature*. **488**, 522–526 (2012).
6. A. Eramo, L. Ricci-Vitiani, A. Zeuner, R. Pallini, F. Lotti, G. Sette, E. Pilozzi, L. M. Larocca, C. Peschle, R. De Maria, Chemotherapy resistance of glioblastoma stem cells. *Cell Death Differ.* **13**, 1238–1241 (2006).
7. Z. Wang, H. Zhang, S. Xu, Z. Liu, Q. Cheng, The adaptive transition of glioblastoma stem cells and its implications on treatments. *Signal Transduct. Target. Ther.* **6**, 124 (2021).
8. D. Garnier, O. Renoult, M.-C. Alves-Guerra, F. Paris, C. Pecqueur, Glioblastoma Stem-

bioRxiv preprint doi: https://doi.org/10.1101/2024.02.02.578510; this version posted February 7, 2024. The copyright holder for this preprint (which was not certified by peer review) is the author/funder, who has granted bioRxiv a license to display the preprint in perpetuity. It is made available under aCC-BY-NC-ND 4.0 International license.

Like Cells, Metabolic Strategy to Kill a Challenging Target. *Front. Oncol.* **9** (2019), doi:10.3389/fonc.2019.00118.

9. A. Segerman, M. Niklasson, C. Haglund, T. Bergström, M. Jarvius, Y. Xie, A. Westermark, D. Sönmez, A. Hermansson, M. Kastemar, Z. Naimaie-Ali, F. Nyberg, M. Berglund, M. Sundström, G. Hesselager, L. Uhrbom, M. Gustafsson, R. Larsson, M. Fryknäs, B. Segerman, B. Westermark, Clonal Variation in Drug and Radiation Response among Glioma-Initiating Cells Is Linked to Proneural-Mesenchymal Transition. *Cell Rep.* **17**, 2994–3009 (2016).

10. Z. Azam, S.-S. T. TO, B. A. Tannous, Mesenchymal Transformation: The Rosetta Stone of Glioblastoma Pathogenesis and Therapy Resistance. *Adv. Sci.* **7**, 2002015 (2020).

11. L. Wang, J. Jung, H. Babikir, K. Shamardani, S. Jain, X. Feng, N. Gupta, S. Rosi, S. Chang, D. Raleigh, D. Solomon, J. J. Phillips, A. A. Diaz, A single-cell atlas of glioblastoma evolution under therapy reveals cell-intrinsic and cell-extrinsic therapeutic targets. *Nat. Cancer*. **3**, 1534–1552 (2022).

12. N. Vasan, J. Baselga, D. M. Hyman, A view on drug resistance in cancer. *Nature*. **575**, 299–309 (2019).

13. C. Holohan, S. Van Schaeybroeck, D. B. Longley, P. G. Johnston, Cancer drug resistance : an evolving paradigm. *Nat. Publ. Gr.* **13**, 714–726 (2013).

14. K. P. L. Bhat, V. Balasubramaniyan, B. Vaillant, R. Ezhilarasan, K. Hummelink, F. Hollingsworth, K. Wani, L. Heathcock, J. D. James, L. D. Goodman, S. Conroy, L. Long, N. Lelic, S. Wang, J. Gumin, D. Raj, Y. Kodama, A. Raghunathan, A. Olar, K. Joshi, C. E. Pelloski, A. Heimberger, S. H. Kim, D. P. Cahill, G. Rao, W. F. A. Den Dunnen, H. W. G. M. Boddeke, H. S. Phillips, I. Nakano, F. F. Lang, H. Colman, E. P. Sulman, K. Aldape, Mesenchymal differentiation mediated by NF-κB promotes radiation resistance in glioblastoma. *Cancer Cell*. **24**, 331–346 (2013).

15. J. Halliday, K. Helmy, S. S. Pattwell, K. L. Pitter, Q. LaPlant, T. Ozawa, E. C. Holland, *Proc. Natl. Acad. Sci.*, doi:10.1073/pnas.1321014111.

16. Z.-D. Shi, K. Pang, Z.-X. Wu, Y. Dong, L. Hao, J.-X. Qin, W. Wang, Z.-S. Chen, C.-H. Han, Tumor cell plasticity in targeted therapy-induced resistance: mechanisms and new strategies. *Signal Transduct. Target. Ther.* **8**, 113 (2023).

17. Y. Sun, B.-E. Wang, K. G. Leong, P. Yue, L. Li, S. Jhunjhunwala, D. Chen, K. Seo, Z. Modrusan, W.-Q. Gao, J. Settleman, L. Johnson, Androgen Deprivation Causes Epithelial–Mesenchymal Transition in the Prostate: Implications for Androgen-Deprivation Therapy. *Cancer Res.* **72**, 527–536 (2012).

bioRxiv preprint doi: https://doi.org/10.1101/2024.02.02.578510; this version posted February 7, 2024. The copyright holder for this preprint (which was not certified by peer review) is the author/funder, who has granted bioRxiv a license to display the preprint in perpetuity. It is made available under aCC-BY-NC-ND 4.0 International license.

18. K. Izumi, L.-Y. Fang, A. Mizokami, M. Namiki, L. Li, W.-J. Lin, C. Chang, Targeting the androgen receptor with siRNA promotes prostate cancer metastasis through enhanced macrophage recruitment via CCL2/CCR2-induced STAT3 activation. *EMBO Mol. Med.* **5**, 1383–1401 (2013).

19. L. Kyjacova, S. Hubackova, K. Krejcikova, R. Strauss, H. Hanzlikova, R. Dzijak, T. Imrichova, J. Simova, M. Reinis, J. Bartek, Z. Hodny, Radiotherapy-induced plasticity of prostate cancer mobilizes stem-like non-adherent, Erk signaling-dependent cells. *Cell Death Differ.* **22**, 898–911 (2015).

20. G. N. Gan, J. Eagles, S. B. Keysar, G. Wang, M. J. Glogowska, C. Altunbas, R. T. Anderson, P. N. Le, J. J. Morton, B. Frederick, D. Raben, X.-J. Wang, A. Jimeno, Hedgehog Signaling Drives Radioresistance and Stroma-Driven Tumor Repopulation in Head and Neck Squamous Cancers. *Cancer Res.* **74**, 7024–7036 (2014).

21. T. Shibue, R. A. Weinberg, EMT, CSCs, and drug resistance: the mechanistic link and clinical implications. *Nat. Rev. Clin. Oncol.* **14**, 611–629 (2017).

22. Z. Culig, Epithelial mesenchymal transition and resistance in endocrine-related cancers. *Biochim. Biophys. Acta - Mol. Cell Res.* **1866**, 1368–1375 (2019).

23. K. Polyak, R. A. Weinberg, Transitions between epithelial and mesenchymal states: acquisition of malignant and stem cell traits. *Nat. Rev. Cancer*. **9**, 265–273 (2009).

24. T. Brabletz, R. Kalluri, M. A. Nieto, R. A. Weinberg, EMT in cancer. *Nat. Rev. Cancer*. **18**, 128–134 (2018).

25. T. B. Steinbichler, J. Dudás, S. Skvortsov, U. Ganswindt, H. Riechelmann, I.-I. Skvortsova, Therapy resistance mediated by cancer stem cells. *Semin. Cancer Biol.* **53**, 156–167 (2018).

26. T. Ozawa, M. Riester, Y.-K. Cheng, J. T. Huse, M. Squatrito, K. Helmy, N. Charles, F. Michor, E. C. Holland, Most Human Non-GCIMP Glioblastoma Subtypes Evolve from a Common Proneural-like Precursor Glioma. *Cancer Cell*. **26**, 288–300 (2014).

27. M. Minata, A. Audia, J. Shi, S. Lu, J. Bernstock, M. S. Pavlyukov, A. Das, S. H. Kim, Y. J. Shin, Y. Lee, H. Koo, K. Snigdha, I. Waghmare, X. Guo, A. Mohyeldin, D. Gallego-Perez, J. Wang, D. Chen, P. Cheng, F. Mukheef, M. Contreras, J. F. Reyes, B. Vaillant, E. P. Sulman, S. Y. Cheng, J. M. Markert, B. A. Tannous, X. Lu, M. Kango-Singh, L. J. Lee, D. H. Nam, I. Nakano, K. P. Bhat, Phenotypic Plasticity of Invasive Edge Glioma Stem-like Cells in Response to Ionizing Radiation. *Cell Rep.* **26**, 1893-1905.e7 (2019).

28. P. Hothi, T. J. Martins, L. Chen, L. Deleyrolle, J.-G. Yoon, B. Reynolds, G. Foltz, High-Throughput Chemical Screens Identify Disulfiram as an Inhibitor of Human Glioblastoma

bioRxiv preprint doi: https://doi.org/10.1101/2024.02.02.578510; this version posted February 7, 2024. The copyright holder for this preprint (which was not certified by peer review) is the author/funder, who has granted bioRxiv a license to display the preprint in perpetuity. It is made available under aCC-BY-NC-ND 4.0 International license.

Stem Cells. *Oncotarget*. **3**, 1124–1136 (2012).

29. P. Jiang, R. Mukthavavam, Y. Chao, I. S. Bharati, V. Fogal, S. Pastorino, X. Cong, N. Nomura, M. Gallagher, T. Abbasi, S. Vali, S. C. Pingle, M. Makale, S. Kesari, Novel anti-glioblastoma agents and therapeutic combinations identified from a collection of FDA approved drugs. *J. Transl. Med.* **12** (2014), doi:10.1186/1479-5876-12-13.

30. P. Jiang, R. Mukthavaram, Y. Chao, N. Nomura, I. S. Bharati, V. Fogal, S. Pastorino, D. Teng, X. Cong, S. C. Pingle, S. Kapoor, K. Shetty, A. Aggrawal, S. Vali, T. Abbasi, S. Chien, S. Kesari, In vitro and in vivo anticancer effects of mevalonate pathway modulation on human cancer cells. *Br. J. Cancer*. **111**, 1562–1571 (2014).

31. S. Lastakchi, M. K. Olaloko, C. McConville, A Potential New Treatment for High-Grade Glioma: A Study Assessing Repurposed Drug Combinations against Patient-Derived High-Grade Glioma Cells. *Cancers (Basel).* **14** (2022).

32. S. Hänzelmann, R. Castelo, J. Guinney, GSVA: gene set variation analysis for microarray and RNA-Seq data. *BMC Bioinformatics*. **14**, 7 (2013).

33. I. Korsunsky, N. Millard, J. Fan, K. Slowikowski, F. Zhang, K. Wei, Y. Baglaenko, M. Brenner, P. Loh, S. Raychaudhuri, Fast, sensitive and accurate integration of single-cell data with Harmony. *Nat. Methods*. **16**, 1289–1296 (2019).

34. L. McInnes, J. Healy, J. Melville, UMAP: Uniform Manifold Approximation and Projection for Dimension Reduction (2020).

35. G. Peyré, M. Cuturi, Computational Optimal Transport: With Applications to Data Science. *Found. Trends® Mach. Learn.* **11**, 355–607 (2019).

36. C. Neftel, J. Laffy, M. G. Filbin, T. Hara, M. E. Shore, G. J. Rahme, A. R. Richman, D. Silverbush, M. L. Shaw, C. M. Hebert, J. Dewitt, S. Gritsch, E. M. Perez, L. N. G. Castro, X. Lan, N. Druck, C. Rodman, D. Dionne, A. Kaplan, M. S. Bertalan, J. Small, K. Pelton, S. Becker, D. Bonal, Q.-D. Nguyen, R. L. Servis, J. M. Fung, R. Mylvaganam, L. Mayr, J. Gojo, C. Haberler, R. Geyeregger, T. Czech, I. Slavc, B. V Nahed, W. T. Curry, B. S. Carter, H. Wakimoto, P. K. Brastianos, T. T. Batchelor, A. Stemmer-Rachamimov, M. Martinez-Lage, M. P. Frosch, I. Stamenkovic, N. Riggi, E. Rheinbay, M. Monje, O. Rozenblatt-Rosen, D. P. Cahill, A. P. Patel, T. Hunter, I. M. Verma, K. L. Ligon, D. N. Louis, A. Regev, B. E. Bernstein, I. Tirosh, M. L. Suvà, An Integrative Model of Cellular States, Plasticity, and Genetics for Glioblastoma. *Cell* (2019), doi:https://doi.org/10.1016/j.cell.2019.06.024.

37. J. Song, EMT or apoptosis: a decision for TGF-β. *Cell Res.* **17**, 289–290 (2007).

38. J. Song, W. Shi, The concomitant apoptosis and EMT underlie the fundamental functions of TGF-β. *Acta Biochim. Biophys. Sin. (Shanghai).* **50**, 91–97 (2017).

bioRxiv preprint doi: https://doi.org/10.1101/2024.02.02.578510; this version posted February 7, 2024. The copyright holder for this preprint (which was not certified by peer review) is the author/funder, who has granted bioRxiv a license to display the preprint in perpetuity. It is made available under aCC-BY-NC-ND 4.0 International license.

39. C. Chen, X. Hao, X. Lai, L. Liu, J. Zhu, H. Shao, D. Huang, H. Gu, T. Zhang, Z. Yu, L. Xie, X. Zhang, Y. Yang, J. Xu, Y. Zhao, Z. Lu, J. Zheng, Oxidative phosphorylation enhances the leukemogenic capacity and resistance to chemotherapy of B cell acute lymphoblastic leukemia. *Sci. Adv.* **7**, eabd6280 (2021).

40. P. Jin, J. Jiang, L. Zhou, Z. Huang, E. C. Nice, C. Huang, L. Fu, Mitochondrial adaptation in cancer drug resistance: prevalence, mechanisms, and management. *J. Hematol. Oncol.* **15**, 97 (2022).

41. Z. Zhang, Y. Tan, C. Huang, X. Wei, Redox signaling in drug-tolerant persister cells as an emerging therapeutic target. *eBioMedicine*. **89**, 104483 (2023).

42. Z. Zhao, Y. Mei, Z. Wang, W. He, The Effect of Oxidative Phosphorylation on Cancer Drug Resistance. *Cancers (Basel).* **15**, 1–17 (2023).

43. J. H. Park, A. H. Feroze, S. N. Emerson, A. B. Mihalas, C. D. Keene, P. J. Cimino, A. L. G. de Lomana, K. Kannan, W. J. Wu, S. Turkarslan, N. S. Baliga, A. P. Patel, A single-cell based precision medicine approach using glioblastoma patient-specific models. *npj Precis. Oncol.* **6** (2022), doi:10.1038/s41698-022-00294-4.

44. C. L. Plaisier, S. O'Brien, B. Bernard, S. Reynolds, Z. Simon, C. M. Toledo, Y. Ding, D. J. Reiss, P. J. Paddison, N. S. Baliga, Causal Mechanistic Regulatory Network for Glioblastoma Deciphered Using Systems Genetics Network Analysis. *Cell Syst.* **3**, 172–186 (2016).

45. D. J. Reiss, N. S. Baliga, R. Bonneau, Integrated biclustering of heterogeneous genome-wide datasets for the inference of global regulatory networks. *BMC Bioinformatics*. **7**, 280 (2006).

46. M. A. Wall, S. Turkarslan, W.-J. Wu, S. A. Danziger, D. J. Reiss, M. J. Mason, A. P. Dervan, M. W. B. Trotter, D. Bassett, R. M. Hershberg, A. L. G. de Lomana, A. V Ratushny, N. S. Baliga, Genetic program activity delineates risk, relapse, and therapy responsiveness in multiple myeloma. *npj Precis. Oncol.* **5**, 60 (2021).

47. C. L. Plaisier, W.-J. Wu, N. S. Baliga, Transcription Factor Target Gene Database (2016), (available at http://tfbsdb.systemsbiology.net/).

48. C. L. Plaisier, M. Pan, N. S. Baliga, A miRNA-regulatory network explains how dysregulated miRNAs perturb oncogenic processes across diverse cancers. *Genome Res.* **22**, 2302–2314 (2012).

49. S. Turkarslan, A. V Raman, A. W. Thompson, C. E. Arens, M. A. Gillespie, F. von Netzer, K. L. Hillesland, S. Stolyar, A. de Lomana, D. J. Reiss, D. Gorman-Lewis, G. M. Zane, J. A. Ranish, J. D. Wall, D. A. Stahl, N. S. Baliga, Mechanism for microbial population collapse

bioRxiv preprint doi: https://doi.org/10.1101/2024.02.02.578510; this version posted February 7, 2024. The copyright holder for this preprint (which was not certified by peer review) is the author/funder, who has granted bioRxiv a license to display the preprint in perpetuity. It is made available under aCC-BY-NC-ND 4.0 International license.

in a fluctuating resource environment. *Mol. Syst. Biol.* **13** (2017), doi:10.15252/msb.20167058.

50. G. MacLeod, D. A. Bozek, N. Rajakulendran, V. Monteiro, M. Ahmadi, Z. Steinhart, M. M. Kushida, H. Yu, F. J. Coutinho, F. M. G. Cavalli, I. Restall, X. Hao, T. Hart, H. A. Luchman, S. Weiss, P. B. Dirks, S. Angers, Genome-Wide CRISPR-Cas9 Screens Expose Genetic Vulnerabilities and Mechanisms of Temozolomide Sensitivity in Glioblastoma Stem Cells. *Cell Rep.* **27**, 971-986.e9 (2019).

51. J. Obacz, T. Avril, P.-J. Le Reste, H. Urra, V. Quillien, C. Hetz, E. Chevet, Endoplasmic reticulum proteostasis in glioblastoma - From molecular mechanisms to therapeutic perspectives. *Sci. Signal.* **10**, eaal2323 (2017).

52. H.-M. Jeon, X. Jin, J.-S. Lee, S.-Y. Oh, Y.-W. Sohn, H.-J. Park, K. M. Joo, W.-Y. Park, D.-H. Nam, R. A. DePinho, L. Chin, H. Kim, Inhibitor of differentiation 4 drives brain tumor-initiating cell genesis through cyclin E and notch signaling. *Genes Dev.* **22**, 2028–2033 (2008).

53. G. La Manno, R. Soldatov, A. Zeisel, E. Braun, H. Hochgerner, V. Petukhov, K. Lidschreiber, M. E. Kastriti, P. Lönnerberg, A. Furlan, J. Fan, L. E. Borm, Z. Liu, D. van Bruggen, J. Guo, X. He, R. Barker, E. Sundström, G. Castelo-Branco, P. Cramer, I. Adameyko, S. Linnarsson, P. V. Kharchenko, RNA velocity of single cells. *Nature*. **560**, 494–498 (2018).

54. V. Bergen, M. Lange, S. Peidli, F. A. Wolf, F. J. Theis, Generalizing RNA velocity to transient cell states through dynamical modeling. *Nat. Biotechnol.* **38**, 1408–1414 (2020).

55. M. Mojtahedi, A. Skupin, J. Zhou, I. G. Casta, Y. Rebecca, H. Chang, K. Trachana, A. Giuliani, S. Huang, Cell Fate Decision as High-Dimensional Critical State Transition. *PLoS Biol.* **14**, 1–28 (2016).

56. G. Gorin, M. Fang, T. Chari, L. Pachter, RNA velocity unraveled. *PLOS Comput. Biol.* **18**, 1–55 (2022).

57. J. Ding, N. Sharon, Z. Bar-Joseph, Temporal modelling using single-cell transcriptomics. *Nat. Rev. Genet.* **23**, 355–368 (2022).

58. M. Fedele, L. Cerchia, S. Pegoraro, R. Sgarra, G. Manfioletti, Proneural-mesenchymal transition: Phenotypic plasticity to acquire multitherapy resistance in glioblastoma. *Int. J. Mol. Sci.* **20** (2019), , doi:10.3390/ijms20112746.

59. D. P. Cook, B. C. Vanderhyden, Transcriptional census of epithelial-mesenchymal plasticity in cancer. *Sci. Adv.* **8** (2022), doi:10.1126/sciadv.abi7640.

60. D. P. Cook, B. C. Vanderhyden, Context specificity of the EMT transcriptional response.

bioRxiv preprint doi: https://doi.org/10.1101/2024.02.02.578510; this version posted February 7, 2024. The copyright holder for this preprint (which was not certified by peer review) is the author/funder, who has granted bioRxiv a license to display the preprint in perpetuity. It is made available under aCC-BY-NC-ND 4.0 International license.

Nat. Commun. **11**, 1–9 (2020).

61. S. Rodríguez-Enríquez, Á. Marín-Hernández, J. C. Gallardo-Pérez, S. C. Pacheco-Velázquez, J. A. Belmont-Díaz, D. X. Robledo-Cadena, J. L. Vargas-Navarro, N. A. de la Peña, E. Saavedra, R. Moreno-Sánchez, Transcriptional Regulation of Energy Metabolism in Cancer Cells. *Cells*. **8** (2019), doi:10.3390/cells8101225.
62. B. Huang, M. Lu, D. Jia, E. Ben-Jacob, H. Levine, J. N. Onuchic, Interrogating the topological robustness of gene regulatory circuits by randomization. *PLOS Comput. Biol.* **13**, 1–21 (2017).
63. B. Huang, D. Jia, J. Feng, H. Levine, J. N. Onuchic, M. Lu, RACIPE: a computational tool for modeling gene regulatory circuits using randomization. *BMC Syst. Biol.* **12**, 74 (2018).
64. V. Kohar, M. Lu, Role of noise and parametric variation in the dynamics of gene regulatory circuits. *npj Syst. Biol. Appl.* **4**, 40 (2018).
65. T. S. Gardner, J. J. Faith, Reverse-engineering transcription control networks. *Phys. Life Rev.* **2**, 65–88 (2005).
66. M. Hecker, S. Lambeck, S. Toepfer, E. van Someren, R. Guthke, Gene regulatory network inference: data integration in dynamic models-a review. *Biosystems.* **96**, 86–103 (2009).
67. M. Banf, S. Y. Rhee, Computational inference of gene regulatory networks: Approaches, limitations and opportunities. *Biochim. Biophys. Acta - Gene Regul. Mech.* **1860**, 41–52 (2017).
68. D. Carvalho-Silva, A. Pierleoni, M. Pignatelli, C. Ong, L. Fumis, N. Karamanis, M. Carmona, A. Faulconbridge, A. Hercules, E. McAuley, A. Miranda, G. Peat, M. Spitzer, J. Barrett, D. G. Hulcoop, E. Papa, G. Koscielny, I. Dunham, Open Targets Platform: new developments and updates two years on. *Nucleic Acids Res.* **47**, D1056–D1065 (2018).
69. J. Bellmunt, C. Théodore, T. Demkov, B. Komyakov, L. Sengelov, G. Daugaard, A. Caty, J. Carles, A. Jagiello-Gruszfeld, O. Karyakin, F.-M. Delgado, P. Hurteloup, E. Winquist, N. Morsli, Y. Salhi, S. Culine, H. von der Maase, Phase III Trial of Vinflunine Plus Best Supportive Care Compared With Best Supportive Care Alone After a Platinum-Containing Regimen in Patients With Advanced Transitional Cell Carcinoma of the Urothelial Tract. *J. Clin. Oncol.* **27**, 4454–4461 (2009).
70. J.-M. Barret, C. Etiévant, B. T. Hill, In vitro synergistic effects of vinflunine, a novel fluorinated vinca alkaloid, in combination with other anticancer drugs. *Cancer Chemother. Pharmacol.* **45**, 471–476 (2000).
71. Y. A. Yabo, S. P. Niclou, A. Golebiewska, Cancer cell heterogeneity and plasticity: A paradigm shift in glioblastoma. *Neuro. Oncol.* **24**, 669–682 (2021).

bioRxiv preprint doi: https://doi.org/10.1101/2024.02.02.578510; this version posted February 7, 2024. The copyright holder for this preprint (which was not certified by peer review) is the author/funder, who has granted bioRxiv a license to display the preprint in perpetuity. It is made available under aCC-BY-NC-ND 4.0 International license.

72. T. M. Ashton, W. G. McKenna, L. A. Kunz-Schughart, G. S. Higgins, Oxidative Phosphorylation as an Emerging Target in Cancer Therapy. *Clin. Cancer Res.* **24**, 2482–2490 (2018).

73. V. Sica, J. M. Bravo-San Pedro, G. Stoll, G. Kroemer, Oxidative phosphorylation as a potential therapeutic target for cancer therapy. *Int. J. Cancer*. **146**, 10–17 (2020).

74. J. P. Thiery, H. Acloque, R. Y. J. Huang, M. A. Nieto, Epithelial-Mesenchymal Transitions in Development and Disease. *Cell*. **139**, 871–890 (2009).

75. A. Dirkse, A. Golebiewska, T. Buder, P. V. Nazarov, A. Muller, S. Poovathingal, N. H. C. Brons, S. Leite, N. Sauvageot, D. Sarkisjan, M. Seyfrid, S. Fritah, D. Stieber, A. Michelucci, F. Hertel, C. Herold-Mende, F. Azuaje, A. Skupin, R. Bjerkvig, A. Deutsch, A. Voss-Böhme, S. P. Niclou, Stem cell-associated heterogeneity in Glioblastoma results from intrinsic tumor plasticity shaped by the microenvironment. *Nat. Commun.* **10** (2019), doi:10.1038/s41467-019-09853-z.

76. K. Leder, K. Pitter, Q. LaPlant, D. Hambardzumyan, B. D. Ross, T. A. Chan, E. C. Holland, F. Michor, Mathematical Modeling of PDGF-Driven Glioblastoma Reveals Optimized Radiation Dosing Schedules. *Cell*. **156**, 603–616 (2014).

77. A. Randles, H.-G. Wirsching, J. A. Dean, Y.-K. Cheng, S. Emerson, S. S. Pattwell, E. C. Holland, F. Michor, Computational modelling of perivascular-niche dynamics for the optimization of treatment schedules for glioblastoma. *Nat. Biomed. Eng.* **5**, 346–359 (2021).

78. I. Larsson, E. Dalmo, R. Elgendy, M. Niklasson, M. Doroszko, A. Segerman, R. Jörnsten, B. Westermark, S. Nelander, Modeling glioblastoma heterogeneity as a dynamic network of cell states. *Mol. Syst. Biol.* **17**, 1–19 (2021).

79. O. Celiku, M. R. Gilbert, O. Lavi, Computational modeling demonstrates that glioblastoma cells can survive spatial environmental challenges through exploratory adaptation. *Nat. Commun.* **10** (2019), doi:10.1038/s41467-019-13726-w.

80. W. Jiang, J.-W. Hu, X.-R. He, W.-L. Jin, X.-Y. He, Statins: a repurposed drug to fight cancer. *J. Exp. Clin. Cancer Res.* **40**, 241 (2021).

81. N. Tilija Pun, N. Lee, S.-H. Song, C.-H. Jeong, Pitavastatin Induces Cancer Cell Apoptosis by Blocking Autophagy Flux. *Front. Pharmacol.* **13**, 854506 (2022).

82. A. K. Altwairgi, F. Alnajjar, H. Alhussain, E. Alsaeed, A. Balbaid, S. Aldandan, Y. Orz, A. Lary, W. Alghareeb, A. Alsharm, 53P - Phase II study of atorvastatin in combination with radiotherapy and temozolomide in patients with glioblastoma (ART): Final analysis report. *Ann. Oncol.* **30**, ix20 (2019).

bioRxiv preprint doi: https://doi.org/10.1101/2024.02.02.578510; this version posted February 7, 2024. The copyright holder for this preprint (which was not certified by peer review) is the author/funder, who has granted bioRxiv a license to display the preprint in perpetuity. It is made available under aCC-BY-NC-ND 4.0 International license.

83. Y. Xie, Q. Lu, C. Lenahan, S. Yang, D. Zhou, X. Qi, Whether statin use improves the survival of patients with glioblastoma?: A meta-analysis. *Medicine (Baltimore).* **99**, e18997 (2020).

84. L. M. Richards, O. K. N. Whitley, G. MacLeod, F. M. G. Cavalli, F. J. Coutinho, J. E. Jaramillo, N. Svergun, M. Riverin, D. C. Croucher, M. Kushida, K. Yu, P. Guilhamon, N. Rastegar, M. Ahmadi, J. K. Bhatti, D. A. Bozek, N. Li, L. Lee, C. Che, E. Luis, N. I. Park, Z. Xu, T. Ketela, R. A. Moore, M. A. Marra, J. Spears, M. D. Cusimano, S. Das, M. Bernstein, B. Haibe-Kains, M. Lupien, H. A. Luchman, S. Weiss, S. Angers, P. B. Dirks, G. D. Bader, T. J. Pugh, Gradient of Developmental and Injury Response transcriptional states defines functional vulnerabilities underpinning glioblastoma heterogeneity. *Nat. Cancer*. **2**, 157–173 (2021).

85. L. Wang, H. Babikir, S. Müller, G. Yagnik, K. Shamardani, F. Catalan, G. Kohanbash, B. Alvarado, E. Di Lullo, A. Kriegstein, S. Shah, H. Wadhwa, S. M. Chang, J. J. Phillips, M. K. Aghi, A. A. Diaz, The phenotypes of proliferating glioblastoma cells reside on a single axis of variation. *Cancer Discov.* **9**, 1708–1719 (2019).

86. H. P. Ellis, M. Greenslade, B. Powell, I. Spiteri, A. Sottoriva, K. M. Kurian, Current Challenges in Glioblastoma: Intratumour Heterogeneity, Residual Disease, and Models to Predict Disease Recurrence. *Front. Oncol.* **5**, 251 (2015).

87. T. Hara, R. Chanoch-Myers, N. D. Mathewson, C. Myskiw, L. Atta, L. Bussema, S. W. Eichhorn, A. C. Greenwald, G. S. Kinker, C. Rodman, L. N. Gonzalez Castro, H. Wakimoto, O. Rozenblatt-Rosen, X. Zhuang, J. Fan, T. Hunter, I. M. Verma, K. W. Wucherpfennig, A. Regev, M. L. Suvà, I. Tirosh, Interactions between cancer cells and immune cells drive transitions to mesenchymal-like states in glioblastoma. *Cancer Cell*. **39**, 779-792.e11 (2021).

88. K. Tsuji, M. Ojima, K. Otabe, M. Horie, H. Koga, I. Sekiya, T. Muneta, Effects of Different Cell-Detaching Methods on the Viability and Cell Surface Antigen Expression of Synovial Mesenchymal Stem Cells. *Cell Transplant.* **26**, 1089–1102 (2017).

89. M. I. Love, W. Huber, S. Anders, Moderated estimation of fold change and dispersion for RNA-seq data with DESeq2. *Genome Biol.* **15**, 550 (2014).

90. T. Stuart, A. Butler, P. Hoffman, C. Hafemeister, E. Papalexi, W. M. Mauck, Y. Hao, M. Stoeckius, P. Smibert, R. Satija, Comprehensive Integration of Single-Cell Data. *Cell*. **177**, 1888-1902.e21 (2019).

91. A. T. L. Lun, K. Bach, J. C. Marioni, Pooling across cells to normalize single-cell RNA sequencing data with many zero counts. *Genome Biol.* **17**, 75 (2016).

bioRxiv preprint doi: https://doi.org/10.1101/2024.02.02.578510; this version posted February 7, 2024. The copyright holder for this preprint (which was not certified by peer review) is the author/funder, who has granted bioRxiv a license to display the preprint in perpetuity. It is made available under aCC-BY-NC-ND 4.0 International license.

92. P. Langfelder, S. Horvath, Eigengene networks for studying the relationships between co-expression modules. *BMC Syst. Biol.* **1**, 54 (2007).

93. C. Trapnell, D. Cacchiarelli, J. Grimsby, P. Pokharel, S. Li, M. Morse, N. J. Lennon, K. J. Livak, T. S. Mikkelsen, J. L. Rinn, The dynamics and regulators of cell fate decisions are revealed by pseudotemporal ordering of single cells. *Nat. Biotechnol.* **32**, 381–6 (2014).

94. J. Cao, M. Spielmann, X. Qiu, X. Huang, D. M. Ibrahim, A. J. Hill, F. Zhang, S. Mundlos, L. Christiansen, F. J. Steemers, C. Trapnell, J. Shendure, The single-cell transcriptional landscape of mammalian organogenesis. *Nature*. **566**, 496–502 (2019).

95. A. Subramanian, P. Tamayo, V. K. Mootha, S. Mukherjee, B. L. Ebert, M. A. Gillette, A. Paulovich, S. L. Pomeroy, T. R. Golub, E. S. Lander, J. P. Mesirov, Gene set enrichment analysis: A knowledge-based approach for interpreting genome-wide expression profiles. *Proc. Natl. Acad. Sci.* **102**, 15545–15550 (2005).

96. M. Janiszewska, M. L. Suvà, N. Riggi, R. H. Houtkooper, J. Auwerx, V. Clément-Schatlo, I. Radovanovic, E. Rheinbay, P. Provero, I. Stamenkovic, Imp2 controls oxidative phosphorylation and is crucial for preserving glioblastoma cancer stem cells. *Genes Dev.* **26**, 1926–1944 (2012).

97. S. Shibao, N. Minami, N. Koike, N. Fukui, K. Yoshida, H. Saya, O. Sampetrean, Metabolic heterogeneity and plasticity of glioma stem cells in a mouse glioblastoma model. *Neuro. Oncol.* **20**, 343–354 (2017).

98. T. Tian, X. Li, J. Zhang, mTOR Signaling in Cancer and mTOR Inhibitors in Solid Tumor Targeting Therapy. *Int. J. Mol. Sci.* **20** (2019), doi:10.3390/ijms20030755.

99. J. H. Hwang, J. H. Seo, M. L. Beshiri, S. Wankowicz, D. Liu, A. Cheung, J. Li, X. Qiu, A. L. Hong, G. Botta, L. Golumb, C. Richter, J. So, G. J. Sandoval, A. O. Giacomelli, S. H. Ly, C. Han, C. Dai, H. Pakula, A. Sheahan, F. Piccioni, O. Gjoerup, M. Loda, A. G. Sowalsky, L. Ellis, H. Long, D. E. Root, K. Kelly, E. M. Van Allen, M. L. Freedman, A. D. Choudhury, W. C. Hahn, CREB5 Promotes Resistance to Androgen-Receptor Antagonists and Androgen Deprivation in Prostate Cancer. *Cell Rep.* **29**, 2355-2370.e6 (2019).

100. J. Lei, M.-H. Zhou, F.-C. Zhang, K. Wu, S.-W. Liu, H.-Q. Niu, Interferon regulatory factor transcript levels correlate with clinical outcomes in human glioma. *Aging (Albany. NY).* **13**, 12086–12098 (2021).

101. N. Meyer-Schaller, S. Tiede, R. Ivanek, M. Diepenbruck, G. Christofori, A dual role of Irf1 in maintaining epithelial identity but also enabling EMT and metastasis formation of breast cancer cells. *Oncogene*. **39**, 4728–4740 (2020).

102. P. Pölönen, A. Jawahar Deen, H. M. Leinonen, H.-K. Jyrkkänen, S. Kuosmanen, M.

bioRxiv preprint doi: https://doi.org/10.1101/2024.02.02.578510; this version posted February 7, 2024. The copyright holder for this preprint (which was not certified by peer review) is the author/funder, who has granted bioRxiv a license to display the preprint in perpetuity. It is made available under aCC-BY-NC-ND 4.0 International license.

Mononen, A. Jain, T. Tuomainen, S. Pasonen-Seppänen, J. M. Hartikainen, A. Mannermaa, M. Nykter, P. Tavi, T. Johansen, M. Heinäniemi, A.-L. Levonen, Nrf2 and SQSTM1/p62 jointly contribute to mesenchymal transition and invasion in glioblastoma. *Oncogene*. **38**, 7473–7490 (2019).

103. F. Bocci, S. C. Tripathi, S. A. Vilchez Mercedes, J. T. George, J. P. Casabar, P. K. Wong, S. M. Hanash, H. Levine, J. N. Onuchic, M. K. Jolly, NRF2 activates a partial epithelial-mesenchymal transition and is maximally present in a hybrid epithelial/mesenchymal phenotype. *Integr. Biol.* **11**, 251–263 (2019).

104. Y. Jiang, J. Zhou, D. Hou, P. Luo, H. Gao, Y. Ma, Y.-S. Chen, L. Li, D. Zou, H. Zhang, Y. Zhang, Z. Jing, Prosaposin is a biomarker of mesenchymal glioblastoma and regulates mesenchymal transition through the TGF-β1/Smad signaling pathway. *J. Pathol.* **249**, 26–38 (2019).

105. A. Ramachandran, P. Vizán, D. Das, P. Chakravarty, J. Vogt, K. W. Rogers, P. Müller, A. P. Hinck, G. P. Sapkota, C. S. Hill, TGF-β uses a novel mode of receptor activation to phosphorylate SMAD1/5 and induce epithelial-to-mesenchymal transition. *Elife*. **7**, 1–29 (2018).

106. X. Chen, H. Li, X. Fan, C. Zhao, K. Ye, Z. Zhao, L. Hu, H. Ma, H. Wang, Z. Fang, Protein Palmitoylation Regulates Cell Survival by Modulating XBP1 Activity in Glioblastoma Multiforme. *Mol. Ther. - Oncolytics*. **17**, 518–530 (2020).

107. S.-F. Tsai, M. Tao, L.-I. Ho, T.-W. Chiou, S.-Z. Lin, H.-L. Su, H.-J. Harn, Isochaihulactone-induced DDIT3 causes ER stress-PERK independent apoptosis in glioblastoma multiforme cells. *Oncotarget*. **8**, 4051–4061 (2017).

108. R. Kalluri, R. A. Weinberg, The basics of epithelial-mesenchymal transition. *J. Clin. Invest.* **119**, 1420–1428 (2009).

109. E. J. Moon, S. S. Mello, C. G. Li, J.-T. Chi, K. Thakkar, J. G. Kirkland, E. L. Lagory, I. J. Lee, A. N. Diep, Y. Miao, M. Rafat, M. Vilalta, L. Castellini, A. J. Krieg, E. E. Graves, L. D. Attardi, A. J. Giaccia, The HIF target MAFF promotes tumor invasion and metastasis through IL11 and STAT3 signaling. *Nat. Commun.* **12**, 4308 (2021).

110. C. Lin, W. Song, X. Bi, J. Zhao, Z. Huang, Z. Li, J. Zhou, J. Cai, H. Zhao, Recent advances in the ARID family: focusing on roles in human cancer. *Onco. Targets. Ther.* **7**, 315–324 (2014).

111. A. Knudson, F. González-Casabianca, A. Feged-Rivadeneira, M. F. Pedreros, S. Aponte, A. Olaya, C. F. Castillo, E. Mancilla, A. Piamba-Dorado, R. Sanchez-Pedraza, M. J. Salazar-Terreros, N. Lucchi, V. Udhayakumar, C. Jacob, A. Pance, M. Carrasquilla, G.

bioRxiv preprint doi: https://doi.org/10.1101/2024.02.02.578510; this version posted February 7, 2024. The copyright holder for this preprint (which was not certified by peer review) is the author/funder, who has granted bioRxiv a license to display the preprint in perpetuity. It is made available under aCC-BY-NC-ND 4.0 International license.

Apráez, J. A. Angel, J. C. Rayner, V. Corredor, Spatio-temporal dynamics of Plasmodium falciparum transmission within a spatial unit on the Colombian Pacific Coast. *Sci. Rep.* **10**, 3756 (2020).

112. B. Wang, H. Guo, H. Yu, Y. Chen, H. Xu, G. Zhao, The Role of the Transcription Factor EGR1 in Cancer. *Front. Oncol.* **11** (2021), doi:10.3389/fonc.2021.642547.

113. Y. Wang, C. Qin, B. Zhao, Z. Li, T. Li, X. Yang, Y. Zhao, W. Wang, EGR1 induces EMT in pancreatic cancer via a P300/SNAI2 pathway. *J. Transl. Med.* **21**, 201 (2023).

114. X. Sun, J. Wang, M. Huang, T. Chen, J. Chen, F. Zhang, H. Zeng, Z. Xu, Y. Ke, STAT3 promotes tumour progression in glioma by inducing FOXP1 transcription. *J. Cell. Mol. Med.* **22**, 5629–5638 (2018).

115. Z.-H. Liu, X.-M. Dai, B. Du, Hes1: a key role in stemness, metastasis and multidrug resistance. *Cancer Biol. Ther.* **16**, 353–359 (2015).

116. S.-C. Wang, X.-L. Lin, H.-Y. Wang, Y.-J. Qin, L. Chen, J. Li, J.-S. Jia, H.-F. Shen, S. Yang, R.-Y. Xie, F. Wei, F. Gao, X.-X. Rong, J. Yang, W.-T. Zhao, T.-T. Zhang, J.-W. Shi, K.-T. Yao, W.-R. Luo, Y. Sun, D. Xiao, Hes1 triggers epithelial-mesenchymal transition (EMT)-like cellular marker alterations and promotes invasion and metastasis of nasopharyngeal carcinoma by activating the PTEN/AKT pathway. *Oncotarget*. **6**, 36713–36730 (2015).

117. A. J. Tsung, M. R. Guda, S. Asuthkar, C. M. Labak, I. J. Purvis, Y. Lu, N. Jain, S. E. Bach, D. V. R. Prasad, K. K. Velpula, Methylation regulates HEY1 expression in glioblastoma. *Oncotarget*. **8**, 44398–44409 (2017).

118. E. Hulleman, M. Quarto, R. Vernell, G. Masserdotti, E. Colli, J. M. Kros, D. Levi, P. Gaetani, P. Tunici, G. Finocchiaro, R. R. y Baena, M. Capra, K. Helin, A role for the transcription factor HEY1 in glioblastoma. *J. Cell. Mol. Med.* **13**, 136–146 (2009).

119. K. K. Nyati, T. Kishimoto, The emerging role of Arid5a in cancer: A new target for tumors. *Genes Dis.*, 1–12 (2022).

120. J. Wang, Y. Chen, Q. Wang, H. Xu, C. Wu, Q. Jiang, G. Wu, H. Zhou, Z. Xiao, Y. Chen, T. Zhang, Q. Lan, MEOX2-mediated regulation of Cathepsin S promotes cell proliferation and motility in glioma. *Cell Death Dis.* **13**, 360 (2022).

121. J. Lee, E. Hoxha, H.-R. Song, A novel NFIA-NFκB feed-forward loop contributes to glioblastoma cell survival. *Neuro. Oncol.* **19**, 524–534 (2017).

122. M. Brun, S. Jain, E. A. Monckton, R. Godbout, Nuclear Factor I Represses the Notch Effector HEY1 in Glioblastoma. *Neoplasia*. **20**, 1023–1037 (2018).

123. Z. Liu, R. Ge, J. Zhou, X. Yang, K. K. Cheng, J. Tao, D. Wu, J. Mao, Nuclear factor IX promotes glioblastoma development through transcriptional activation of Ezrin.

bioRxiv preprint doi: https://doi.org/10.1101/2024.02.02.578510; this version posted February 7, 2024. The copyright holder for this preprint (which was not certified by peer review) is the author/funder, who has granted bioRxiv a license to display the preprint in perpetuity. It is made available under aCC-BY-NC-ND 4.0 International license.

Oncogenesis. **9**, 39 (2020).

124. M. L. Suvà, E. Rheinbay, S. M. Gillespie, A. P. Patel, H. Wakimoto, S. D. Rabkin, N. Riggi, A. S. Chi, D. P. Cahill, B. V Nahed, W. T. Curry, R. L. Martuza, M. N. Rivera, N. Rossetti, S. Kasif, S. Beik, S. Kadri, I. Tirosh, I. Wortman, A. K. Shalek, O. Rozenblatt-Rosen, A. Regev, D. N. Louis, B. E. Bernstein, Reconstructing and reprogramming the tumor-propagating potential of glioblastoma stem-like cells. *Cell*. **157**, 580–594 (2014).

125. A. Ghorai, T. Mahaddalkar, R. Thorat, S. Dutt, Sustained inhibition of PARP-1 activity delays glioblastoma recurrence by enhancing radiation-induced senescence. *Cancer Lett.* **490**, 44–53 (2020).

126. B. Murnyák, M. C. Kouhsari, R. Hershkovitch, B. Kálmán, G. Marko-Varga, Á. Klekner, T. Hortobágyi, PARP1 expression and its correlation with survival is tumour molecular subtype dependent in glioblastoma. *Oncotarget*. **8**, 46348–46362 (2017).

127. M. Kumar, R. K. Jaiswal, R. Prasad, S. S. Yadav, A. Kumar, P. K. Yadava, R. P. Singh, PARP-1 induces EMT in non-small cell lung carcinoma cells via modulating the transcription factors Smad4, p65 and ZEB1. *Life Sci.* **269**, 118994 (2021).

128. M. Ahmed, T. H. Lai, W. Kim, D. R. Kim, A Functional Network Model of the Metastasis Suppressor PEBP1/RKIP and Its Regulators in Breast Cancer Cells. *Cancers (Basel).* **13** (2021), doi:10.3390/cancers13236098.

129. H. Y. Jeong, H.-J. Kim, C.-E. Kim, S. Lee, M.-C. Choi, S.-H. Kim, High expression of RFX4 is associated with tumor progression and poor prognosis in patients with glioblastoma. *Int. J. Neurosci.* **131**, 7–14 (2021).

130. H.-C. Ku, C.-F. Cheng, Master Regulator Activating Transcription Factor 3 (ATF3) in Metabolic Homeostasis and Cancer. *Front. Endocrinol. (Lausanne).* **11** (2020), doi:10.3389/fendo.2020.00556.

131. J. Zhang, H. Jiang, J. Shao, R. Mao, J. Liu, Y. Ma, X. Fang, N. Zhao, S. Zheng, B. Lin, SOX4 inhibits GBM cell growth and induces G0/G1 cell cycle arrest through Akt-p53 axis. *BMC Neurol.* **14**, 207 (2014).

132. N. Tiwari, V. K. Tiwari, L. Waldmeier, P. J. Balwierz, P. Arnold, M. Pachkov, N. Meyer-Schaller, D. Schübeler, E. van Nimwegen, G. Christofori, Sox4 Is a Master Regulator of Epithelial-Mesenchymal Transition by Controlling Ezh2 Expression and Epigenetic Reprogramming. *Cancer Cell*. **23**, 768–783 (2013).

133. I. Kurtsdotter, D. Topcic, A. Karlén, B. Singla, D. W. Hagey, M. Bergsland, P. Siesjö, M. Nistér, J. W. Carlson, V. Lefebvre, O. Persson, J. Holmberg, J. Muhr, SOX5/6/21 Prevent Oncogene-Driven Transformation of Brain Stem Cells. *Cancer Res.* **77**, 4985–4997 (2017).

bioRxiv preprint doi: https://doi.org/10.1101/2024.02.02.578510; this version posted February 7, 2024. The copyright holder for this preprint (which was not certified by peer review) is the author/funder, who has granted bioRxiv a license to display the preprint in perpetuity. It is made available under aCC-BY-NC-ND 4.0 International license.

134. X.-H. Pei, X.-Q. Lv, H.-X. Li, Sox5 induces epithelial to mesenchymal transition by transactivation of Twist1. *Biochem. Biophys. Res. Commun.* **446**, 322–327 (2014).

135. P. Aldaz, N. Martín-Martín, A. Saenz-Antoñanzas, E. Carrasco-Garcia, M. Álvarez-Satta, A. Elúa-Pinin, S. M. Pollard, C. H. Lawrie, M. Moreno-Valladares, N. Samprón, J. Hench, R. Lovell-Badge, A. Carracedo, A. Matheu, High SOX9 Maintains Glioma Stem Cell Activity through a Regulatory Loop Involving STAT3 and PML. *Int. J. Mol. Sci.* **23** (2022), doi:10.3390/ijms23094511.

136. Z. Wang, X. Xu, N. Liu, Y. Cheng, W. Jin, P. Zhang, X. Wang, H. Yang, H. Liu, Y. Tu, SOX9-PDK1 axis is essential for glioma stem cell self-renewal and temozolomide resistance. *Oncotarget*. **9**, 192–204 (2018).

137. J.-Q. Huang, F.-K. Wei, X.-L. Xu, S.-X. Ye, J.-W. Song, P.-K. Ding, J. Zhu, H.-F. Li, X.-P. Luo, H. Gong, L. Su, L. Yang, L.-Y. Gong, SOX9 drives the epithelial–mesenchymal transition in non-small-cell lung cancer through the Wnt/β-catenin pathway. *J. Transl. Med.* **17**, 143 (2019).

138. B. Weigle, R. Ebner, A. Temme, S. Schwind, M. Schmitz, A. Kiessling, M. A. Rieger, G. Schackert, H. K. Schackert, E. P. Rieber, Highly specific overexpression of the transcription factor SOX11 in human malignant gliomas. *Oncol. Rep.* **13**, 139–144 (2005).

139. B. Wang, Q. Ma, X. Wang, K. Guo, Z. Liu, G. Li, TGIF1 overexpression promotes glioma progression and worsens patient prognosis. *Cancer Med.* (2022).

140. C.-C. Weng, M.-J. Hsieh, C.-C. Wu, Y.-C. Lin, Y.-S. Shan, W.-C. Hung, L.-T. Chen, K.-H. Cheng, Loss of the transcriptional repressor TGIF1 results in enhanced Kras-driven development of pancreatic cancer. *Mol. Cancer*. **18**, 96 (2019).

141. M. S. Carro, W. K. Lim, M. J. Alvarez, R. J. Bollo, X. Zhao, E. Y. Snyder, E. P. Sulman, S. L. Anne, F. Doetsch, H. Colman, A. Lasorella, K. Aldape, A. Califano, A. Iavarone, The transcriptional network for mesenchymal transformation of brain tumours. *Nature*. **463**, 318–25 (2010).

142. Y.-H. Tseng, Y.-H. Huang, T.-K. Lin, S.-M. Wu, H.-C. Chi, C.-Y. Tsai, M.-M. Tsai, Y.-H. Lin, W.-C. Chang, Y.-T. Chang, W.-J. Chen, K.-H. Lin, Thyroid hormone suppresses expression of stathmin and associated tumor growth in hepatocellular carcinoma. *Sci. Rep.* **6**, 38756 (2016).

143. X. Ruan, R. Zhang, R. Li, H. Zhu, Z. Wang, C. Wang, Z. Cheng, H. Peng, The Research Progress in Physiological and Pathological Functions of TRAF4. *Front. Oncol.* **12**, 1–13 (2022).

144. A. C. Liu, D. K. Welsh, C. H. Ko, H. G. Tran, E. E. Zhang, A. a. Priest, E. D. Buhr, O. Singer,

bioRxiv preprint doi: https://doi.org/10.1101/2024.02.02.578510; this version posted February 7, 2024. The copyright holder for this preprint (which was not certified by peer review) is the author/funder, who has granted bioRxiv a license to display the preprint in perpetuity. It is made available under aCC-BY-NC-ND 4.0 International license.

1634 K. Meeker, I. M. Verma, F. J. Doyle, J. S. Takahashi, S. a. Kay, Intercellular Coupling
1635 Confers Robustness against Mutations in the SCN Circadian Clock Network. *Cell*. **129**,
1636 605–616 (2007).
1637 145. L. Zhang, F. Zhou, A. G. de Vinuesa, E. M. de Kruijf, W. E. Mesker, L. Hui, Y. Drabsch, Y.
1638 Li, A. Bauer, A. Rousseau, K.-A. Sheppard, C. Mickanin, P. J. K. Kuppen, C. X. Lu, P. ten
1639 Dijke, TRAF4 Promotes TGF-β Receptor Signaling and Drives Breast Cancer Metastasis.
1640 *Mol. Cell*. **51**, 559–572 (2013).
1641 146. D. Chen, M. Rauh, M. Buchfelder, I. Y. Eyupoglu, N. Savaskan, The oxido-metabolic driver
1642 ATF4 enhances temozolamide chemo-resistance in human gliomas. *Oncotarget*. **8**,
1643 51164–51176 (2017).
1644 147. N. I. Lorenz, A. C. M. Sittig, H. Urban, A.-L. Luger, A. L. Engel, C. Münch, J. P. Steinbach,
1645 M. W. Ronellenfitsch, Activating transcription factor 4 mediates adaptation of human
1646 glioblastoma cells to hypoxia and temozolomide. *Sci. Rep.* **11**, 14161 (2021).
1647 148. Z. Renfro, B. E. White, K. E. Stephens, CCAAT enhancer binding protein gamma (C/EBP-
1648 γ): An understudied transcription factor. *Adv. Biol. Regul.* **84**, 100861 (2022).
1649 149. L. Sampieri, P. Di Giusto, C. Alvarez, CREB3 transcription factors: ER-golgi stress
1650 transducers as hubs for cellular homeostasis. *Front. Cell Dev. Biol.* **7**, 1–13 (2019).
1651 150. K. Hari, B. Sabuwala, B. V. Subramani, C. A. M. La Porta, S. Zapperi, F. Font-Clos, M. K.
1652 Jolly, Identifying inhibitors of epithelial–mesenchymal plasticity using a network topology-
1653 based approach. *npj Syst. Biol. Appl.* **6**, 15 (2020).
1654 151. L. Chauhan, U. Ram, K. Hari, M. K. Jolly, Topological signatures in regulatory network
1655 enable phenotypic heterogeneity in small cell lung cancer. *Elife*. **10**, e64522 (2021).
1656 152. Y.-C. Lin, J.-H. Lin, C.-W. Chou, Y.-F. Chang, S.-H. Yeh, C.-C. Chen, Statins increase p21
1657 through inhibition of histone deacetylase activity and release of promoter-associated
1658 HDAC1/2. *Cancer Res.* **68**, 2375–2383 (2008).
1659 153. N. Mohammadzadeh, F. Montecucco, F. Carbone, S. Xu, K. Al-Rasadi, A. Sahebkar,
1660 Statins: Epidrugs with effects on endothelial health? *Eur. J. Clin. Invest.* **50**, e13388 (2020).
1661 154. S. Bridgeman, W. Northrop, G. Ellison, T. Sabapathy, P. E. Melton, P. Newsholme, C. D.
1662 S. Mamotte, Statins Do Not Directly Inhibit the Activity of Major Epigenetic Modifying
1663 Enzymes. *Cancers (Basel).* **11** (2019), doi:10.3390/cancers11040516.
1664 155. E. Rampazzo, L. Manfreda, S. Bresolin, A. Cani, E. Mariotto, R. Bortolozzi, A. Della Puppa,
1665 G. Viola, L. Persano, Histone Deacetylase Inhibitors Impair Glioblastoma Cell Motility and
1666 Proliferation. *Cancers (Basel).* **14** (2022), doi:10.3390/cancers14081897.
1667

bioRxiv preprint doi: https://doi.org/10.1101/2024.02.02.578510; this version posted February 7, 2024. The copyright holder for this preprint (which was not certified by peer review) is the author/funder, who has granted bioRxiv a license to display the preprint in perpetuity. It is made available under aCC-BY-NC-ND 4.0 International license.

FIGURE LEGENDS

Fig. 1. Pitavastatin causes shift in molecular subtype expressed by PD-GSCs. (A) Pitavastatin IC_{50} values for each of 45 PD-GSCs as determined using dose titration assays (below). Labeled PD-GSCs represent a subset deemed as a responders (blue) and non-responders (red) to pitavastatin. Below are drug-dose response and time-course response curves for SN520 (pitavastatin-responsive) and SN503 (pitavastatin-non-responsive) PD-GSC populations. **(B)** Experimental workflow for longitudinal monitoring of PD-GSC response to pitavastatin treatment. Colored horizontal arrows indicate duration of pitavastatin (magenta), vehicle-control (DMSO, light blue), or untreated control (dark grey). **(C)** GSVA enrichment scores for each molecular subtype (CL – classical, PN – proneural, MES – mesenchymal) analyzed for all bulk samples collected. **(D)** UMAP plots of Harmony-integrated scRNA-seq data sets and corresponding individual plots for each PD-GSC phenotype treated with DMSO or pitavastatin (PSTAT) and untreated controls (CTRL) representing D0 time point. **(E)** Wasserstein distance of transport distances between each consecutive time point for each PD-GSC under each treatment condition (vehicle- or pitavastatin-treatment).

Fig. 2. Single-cell characterization of PD-GSC response to pitavastatin. UMAP plots of scRNA-seq profiles, annotated according to treatment conditions (untreated control, vehicle – DMSO, and pitavastatin – PSTAT), for **(A)** SN520 and **(B)** SN503. Scatter plots show proportions of each subtype in each PD-GSC population across treatment for **(C)** SN520 and **(D)** SN503. **(E – F)** Flow cytometry analysis of PN and MES markers CD133 (PN) and CD44 (MES) across pitavastatin-treated cells for SN520 and SN503, respectively. Values (grey) indicate percentages of cell populations in each quadrant. Proportions of cells positive for each subtype marker are quantified in the adjacent barplots underneath. **(G – H)** Heatmap of inferCNV scores for SN520 and SN503, respectively. Cells (rows) are grouped based on treatment conditions (same color annotation as in (A) and (B)). Genes (columns) are arranged according to their chromosomal positions. **(I)** Dose-response curves of naïve SN520 PD-GSCs (light blue) and SN520 PD-GSCs that survived an initial pitavastatin-treatment (treated – dark blue). Adjacent plot shows corresponding AUC values from dose-response curves generated from subsequent PD-GSC cultures derived from original pitavastatin- or vehicle-control-treatment for SN520 (left) and SN503 (right). Paired t-test results showed a sustained (significant) increase in AUC values of the PSTAT-treated SN520 PD-GSCs relative to their vehicle-control counterparts but not for SN503.

bioRxiv preprint doi: https://doi.org/10.1101/2024.02.02.578510; this version posted February 7, 2024. The copyright holder for this preprint (which was not certified by peer review) is the author/funder, who has granted bioRxiv a license to display the preprint in perpetuity. It is made available under aCC-BY-NC-ND 4.0 International license.

Fig. 3. Differential expression and pathway enrichment analysis reveals underlying processes driving pitavastatin responses. (A) Heatmap of the top upregulated DEGs, based on FDR p-values, across the 14 Louvain cell clusters (cl) identified in vehicle-control- and pitavastatin-treated SN520 PD-GSCs. Adjacent UMAP plot with treatment annotation (same as Fig 2A) included for reference. **(B)** Corresponding UMAP plots of scRNA-seq profiles annotated according to Louvain cell cluster (left) and treatment condition (right) as reference. **(C)** Cell proportions for each Louvain cluster that belong to each treatment condition for SN520. Significant enrichment of treatment condition within Louvain cluster indicated by asterisk (FDR $\leq$ 0.05) or double dagger (FDR $\leq$ 1e-05) **(D)** Cell proportions for each Louvain cluster that belong to each treatment condition for SN503. Significant enrichment notation identical to that used in (D). **(E)** Dotplot of hallmark gene sets enriched across SN503 and SN520 PD-GSCs, grouped with respect to either drug-treatment duration or Louvain clustering. Dot size represents the ratio of number of upregulated genes associated with a PD-GSC grouping to the number of genes associated with a specific hallmark gene set. Dot colors indicate significance of enrichment (FDR value). **(F)** Total number of up- and down-regulated DEGs, relative to untreated control (D0) cells, at each treatment time point for SN503 (red) and SN520 (blue).

Fig. 4. MINER3 transcriptional regulatory network inference reveals mechanisms of cell-state changes. **(A)** Heatmaps of normalized regulon activities across SN520 (top) and SN503 (bottom) PD-GSCs. Regulons (rows) are organized into transcriptional programs (Pr) while single cells (columns) are organized into transcriptional states (St). Left-adjacent color bars indicate what regulons belong to a particular transcriptional program. Left-adjacent color bar indicates transcriptional programs. Top color bars indicate treatment condition (color annotation identical to Fig. 1E) and corresponding transcriptional state for a single cell. (**B)** Stacked barplot show proportion of cells within each transcriptional state from each treatment condition for SN520 (top) and SN503 (bottom). **(C)** Boxplot/violin plots of distributions of regulon activity for select programs across treatment conditions for SN520 and SN503. Regulon activity values were capped between the lower 2.5% and 97.5% range of values. Labels indicate program IDs and select hallmark gene sets (*95*) enriched within each program. The box represents the inter-quantile range (IQR – 25th and 75th percentile) and median activity value while the whiskers represent 1.5x IQR. Asterisks indicate statistically significant differences between regulon activity distributions. Single asterisks (*) denote activity distribution of untreated controls (CTRL) is significantly lower than distribution being compared (FDR << 1e-3). Double asterisks (**) denote distribution of untreated controls is significantly higher than either vehicle-treated (DMSO) or pitavstatin-treated (PSTAT)

bioRxiv preprint doi: https://doi.org/10.1101/2024.02.02.578510; this version posted February 7, 2024. The copyright holder for this preprint (which was not certified by peer review) is the author/funder, who has granted bioRxiv a license to display the preprint in perpetuity. It is made available under aCC-BY-NC-ND 4.0 International license.

distributions being compared (FDR << 1e-3). **(D)** Flow diagram outlining approach to derive core TF-TF network from MINER3 results. Final core TF-TF networks derived for **(E)** SN520 and **(F)** SN503.

Fig. 5. Distinct trajectories define SN520 and SN503 pitavastatin response. (A) UMAP plots of vehicle- and pitavastatin-treated cells for SN520 (left column) and SN503 (right column). Annotation highlights treatment conditions (top row), molecular subtype (2nd row), pseudotime (3rd row) and RNA velocity (4th row). **(B)** Critical transition index (I_c) of SN520 (blue) and SN503 (red) cells treated with vehicle (DMSO - light) or pitavastatin (PSTAT – dark). **(C)** LOESS regression of TF expression behavior sorted according to peak expression along pseudotime (Monocle3). Density plots depict distribution of sample time points along pseudotime trajectory. Heatmap shows expression of TFs rank sorted by time of peak expression along pseudotime (color bar beneath heatmap). **(D)** Select set of LOESS regression of mean program activities with respect to pseudotime. Regulons are clustered based on their dynamic activity profiles with respect to pseudotime. Dashed grey line represents the average shape of the curves for each cluster. Labels indicate which transcriptional programs were grouped into each cluster. Select hallmark gene sets (*95*) enriched within programs are labeled as well. **(E)** Boxplots/violin plots of expression of genes associated with indicated pathways/processes (*95*) on respective treatment days. Relative gene expression values were capped at the lower 2.5% and 97.5% range of values. Labels indicate select hallmark gene sets enriched within subpopulation of cells (treatment time point). Asterisks indicate statistically greater expression in pitavstatin-treated cells (PSTAT) relative to untreated control (CTRL) counterparts (Wilcoxon rank test, FDR << 1e-5). The box represents the inter-quantile range (IQR – 25th and 75th percentile), median activity value while the whiskers highlight 1.5x IQR.

Fig. 6. Dynamic simulations of core TF regulatory network supports phenotypic plasticity of GSCs. Simulated transcriptional states (black circles) projected along first two principal components. Contour lines represent distribution of PCA scores of TF expression states (core TFs only) for **(A)** SN520 and **(B)** SN503 cells. One thousand simulated states were generated using core TF network topologies and corresponding D0 scRNA-seq data for initial conditions (i.c.) as RACIPE inputs. **(C)** Three plots summarizing results from 1 million RACIPE simulations (independent of (A)) using the core TF-TF network derived from scSYGNAL-520 and randomized initial conditions to explore plausible steady states supported by the network topology. Dendrogram of four distinct simulated steady states. Scatter plot of simulated states projected

bioRxiv preprint doi: https://doi.org/10.1101/2024.02.02.578510; this version posted February 7, 2024. The copyright holder for this preprint (which was not certified by peer review) is the author/funder, who has granted bioRxiv a license to display the preprint in perpetuity. It is made available under aCC-BY-NC-ND 4.0 International license.

along first two PCs. Horizontal barplot of rank-ordered TFs based on their importance in distinguishing the four simulated states. Here, importance is defined by the mean decrease in classification accuracy following TF removal from the model, per random forest analysis. **(D)** Heatmap of expression for SN520 core TFs. Cells (columns) were hierarchically clustered to define experimental states (ES_{520}-*i*), providing a basis of comparison for simulated states (SS_{520}-*i*). Adjacent boxplots of three TFs having high importance in random forest classification. Boxplots (top row) of TF expression distributions for experimental states. Boxplots (bottom row) of simulated TF expression distributions (normalized). **(E – F)** Corresponding simulation results for SN503. **(G)** SN520 cell viability following 4-day treatment with either simultaneous treatment with pitavastatin and siRNA (light grey bars) or sequential pitavastatin then siRNA-mediated KD of TFs (dark gray bars). Viabilities are relative to non-template control (NTC)-treated cells. **(H)** Corresponding bar plots of relative viability for SN503. Asterisks (G – H) indicate significant decrease relative to corresponding NTC treatment (FDR p-values $\leq$ 0.1).

Fig. 7. Dynamics of regulon behavior reveal additional targets that guide rational secondary drug selection. Distribution of activity of select tubulin-associated regulons in single cells across treatments for **(A)** SN520 and **(B)** SN503. Asterisks indicate treatments having significantly higher activities relative to the untreated control (CTRL (D0)) (Wilcoxon rank test, $*$ FDR $\leq$ 1e-20, $**$ FDR $\leq$ 1e-150). **(C)** Experimental design for sequential pitavastatin/vinflunine treatment on multiple PD-GSCs. **(D)** Dose-response curves for SN520 and SN503 cells treated with pitavastatin alone (PIT, dark gray), or pre-treated with vehicle (DMSO, light blue)/pitavastatin (2μM, pink), followed by 24hr vinflunine treatment (1.5e-9, 4.6e-9, 13.7e-9, 41.2e-9, 123.5e-9, 370.4e-9, 1.10e-6, 3.30e-6, 10.0e-6 30.0e-6 M). Results from 48hr vinflunine treatment included in fig. S16. Adjacent barplots show relative viabilities following various treatments (black dots underneath barplots) including monotherapy with pitavastatin (PIT), or pre-treatment with DMSO (pre-DMSO)/pitavastatin (pre-PIT) followed by vinflunine (VIN). Asterisks/double crosses indicate treatments resulting in significantly lower relative viability than pitavastatin monotherapy ($*$ 1.1μM, FDR $\leq$ 0.1; ‡ 3.3 μM FDR $\leq$ 0.1). Color annotation identical to dose-response curves. Error bars represent $\pm$2x standard deviation (N = 3). **(E)** Depiction of how core TF-TF networks underlying drug-response drive cell state transitions in responder and non-responder PD-GSCs along a Waddington-like phenotypic landscape. Treatment with a primary drug to which cells are sensitive (1° $drug^S$) activates a highly interconnected network in a responder PD-GSC, driving PMT across surviving cells resulting in acquired resistance to "multiple $drugs^R$". Intervention with a second drug (2° $drug^S$) that targets vulnerabilities in transient states potentiates killing and disrupts PMT.

bioRxiv preprint doi: https://doi.org/10.1101/2024.02.02.578510; this version posted February 7, 2024. The copyright holder for this preprint (which was not certified by peer review) is the author/funder, who has granted bioRxiv a license to display the preprint in perpetuity. It is made available under aCC-BY-NC-ND 4.0 International license.

By contrast, the non-responder PD-GSC consists of cell sub-populations (center well) resistant to the primary drug (1° $drug^R$). Here, treatment with 1° $drug^R$ activates a sparse network that drives surviving cells into multiple distinct drug-resistant states potentially sensitive to secondary interventions.

SUPPLEMENTARY MATERIALS

Supplementary Text

Figs. S1 to S17

Tables S1 to S16

bioRxiv preprint doi: https://doi.org/10.1101/2024.02.02.578510; this version posted February 7, 2024. The copyright holder for this preprint (which was not certified by peer review) is the author/funder, who has granted bioRxiv a license to display the preprint in perpetuity. It is made available under aCC-BY-NC-ND 4.0 International license.

Figure 1

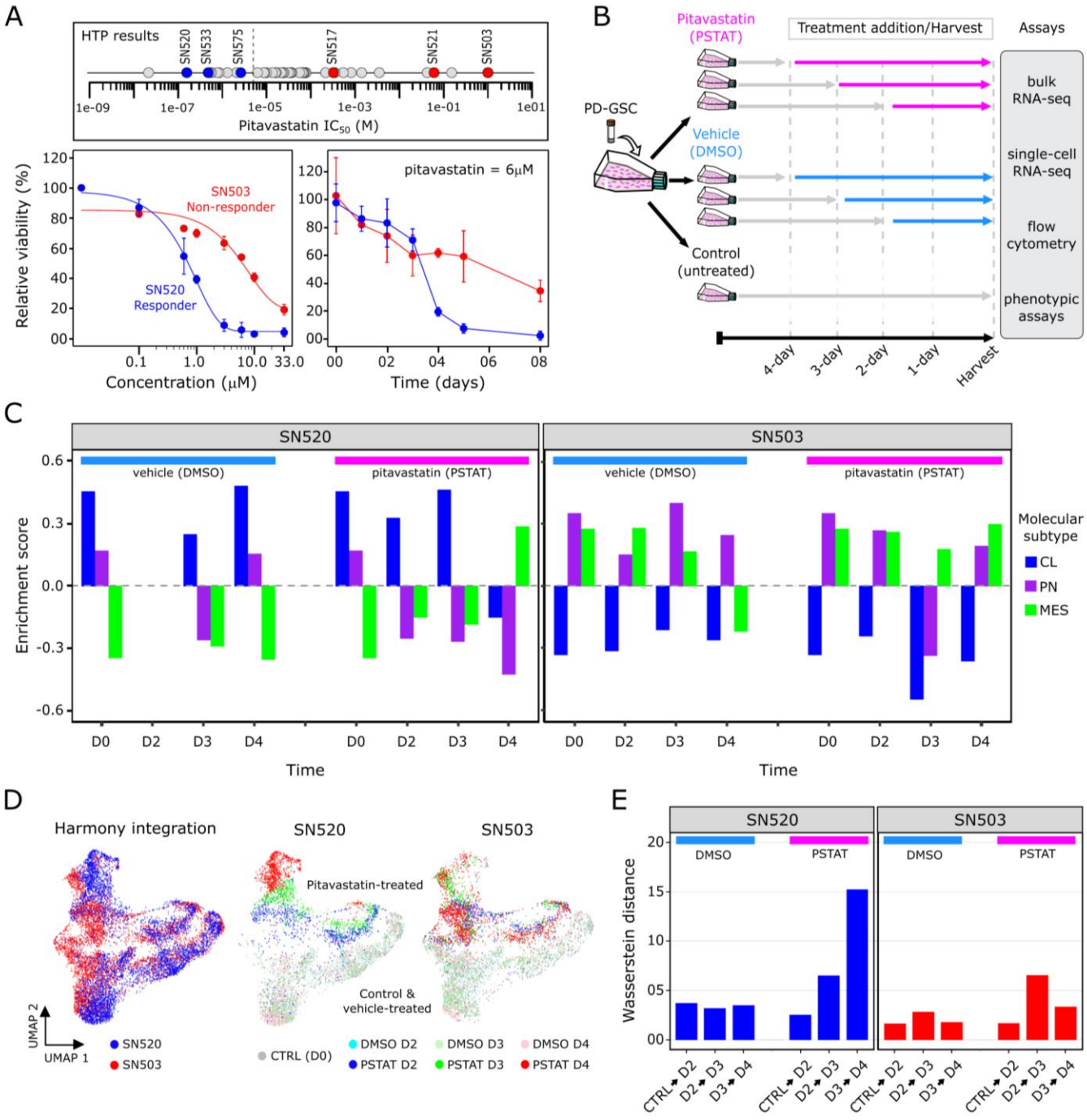

bioRxiv preprint doi: https://doi.org/10.1101/2024.02.02.578510; this version posted February 7, 2024. The copyright holder for this preprint (which was not certified by peer review) is the author/funder, who has granted bioRxiv a license to display the preprint in perpetuity. It is made available under aCC-BY-NC-ND 4.0 International license.

Figure 2

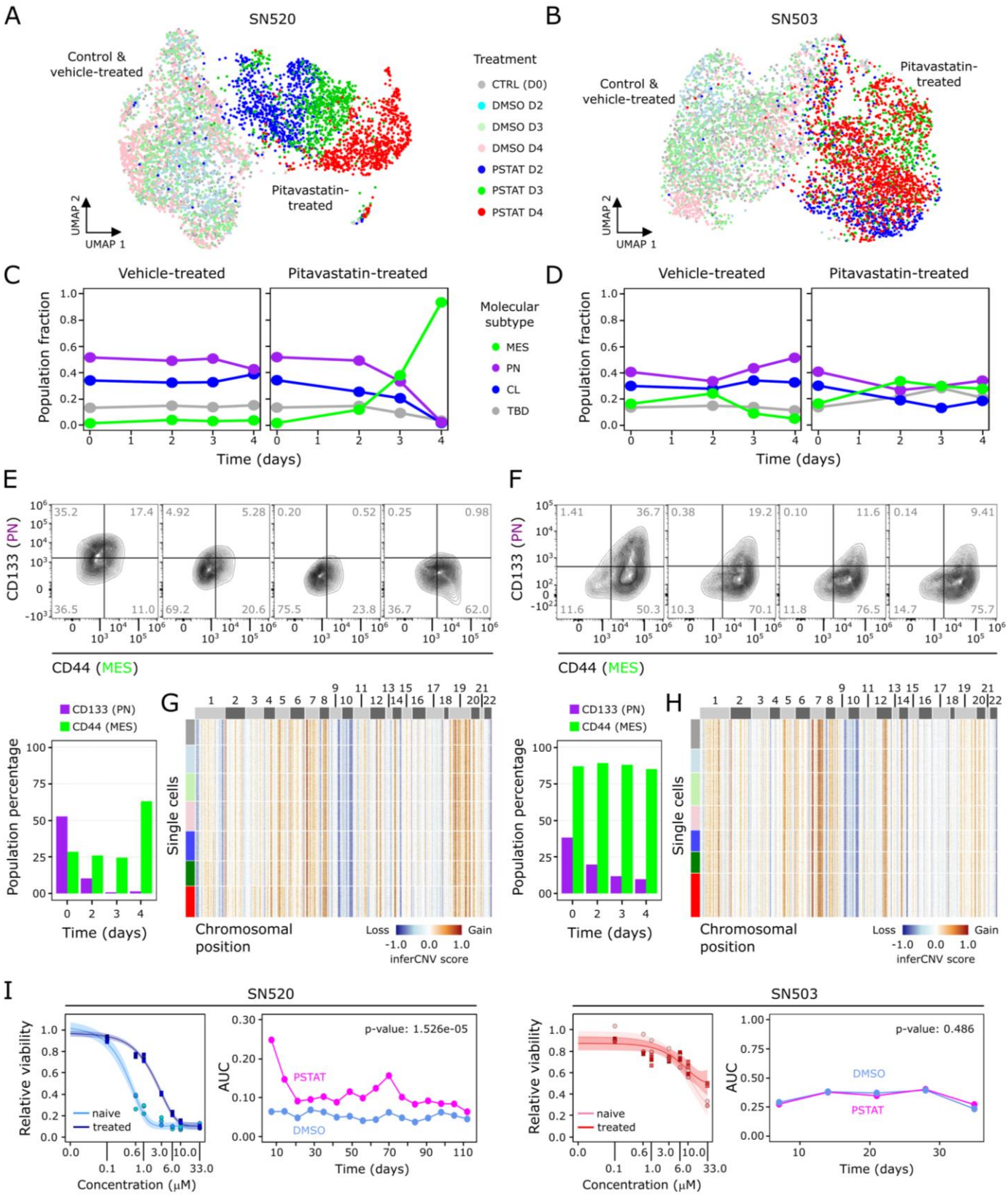

817

bioRxiv preprint doi: https://doi.org/10.1101/2024.02.02.578510; this version posted February 7, 2024. The copyright holder for this preprint (which was not certified by peer review) is the author/funder, who has granted bioRxiv a license to display the preprint in perpetuity. It is made available under aCC-BY-NC-ND 4.0 International license.

Figure 3

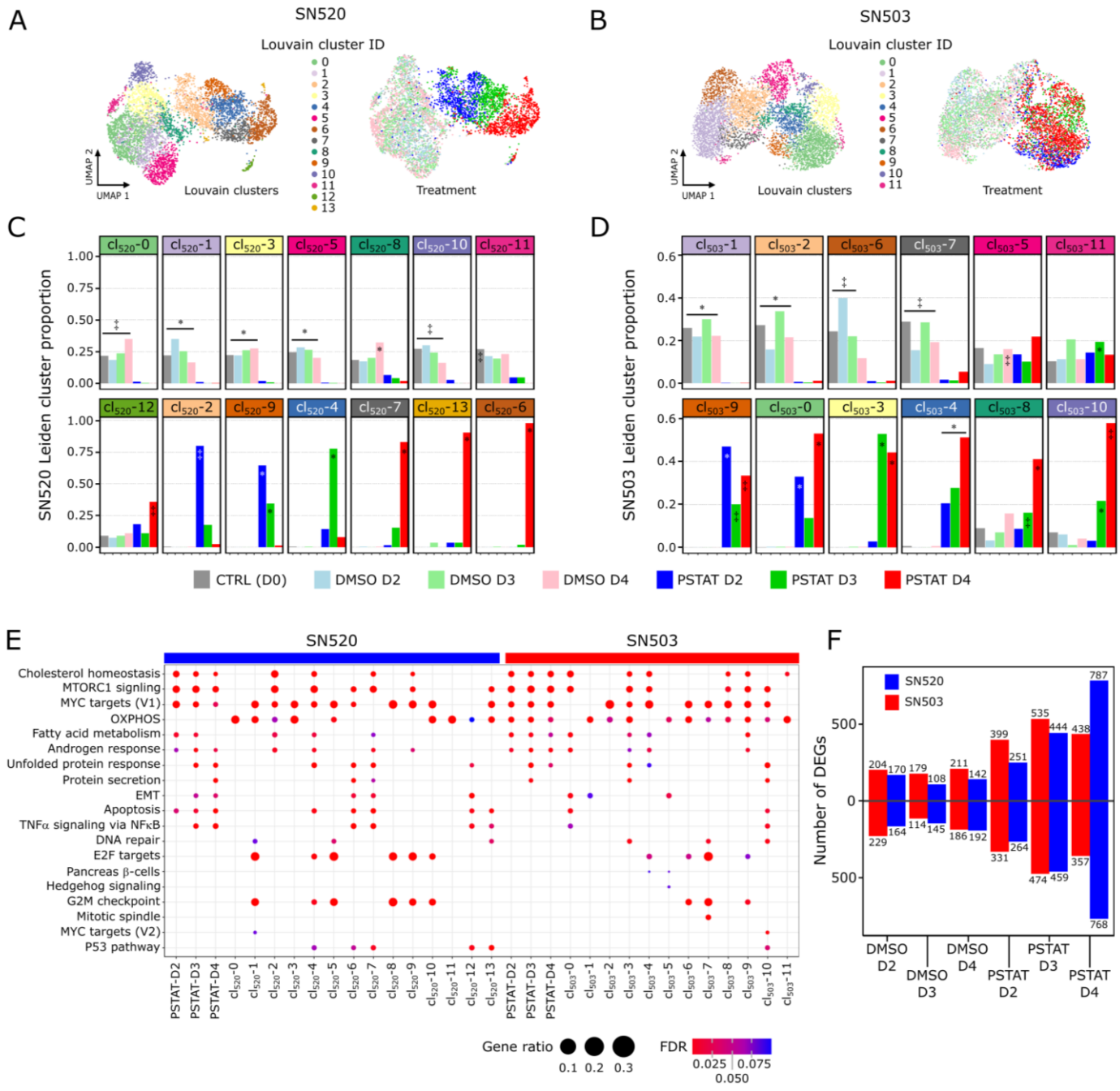

bioRxiv preprint doi: https://doi.org/10.1101/2024.02.02.578510; this version posted February 7, 2024. The copyright holder for this preprint (which was not certified by peer review) is the author/funder, who has granted bioRxiv a license to display the preprint in perpetuity. It is made available under aCC-BY-NC-ND 4.0 International license.

Figure 4

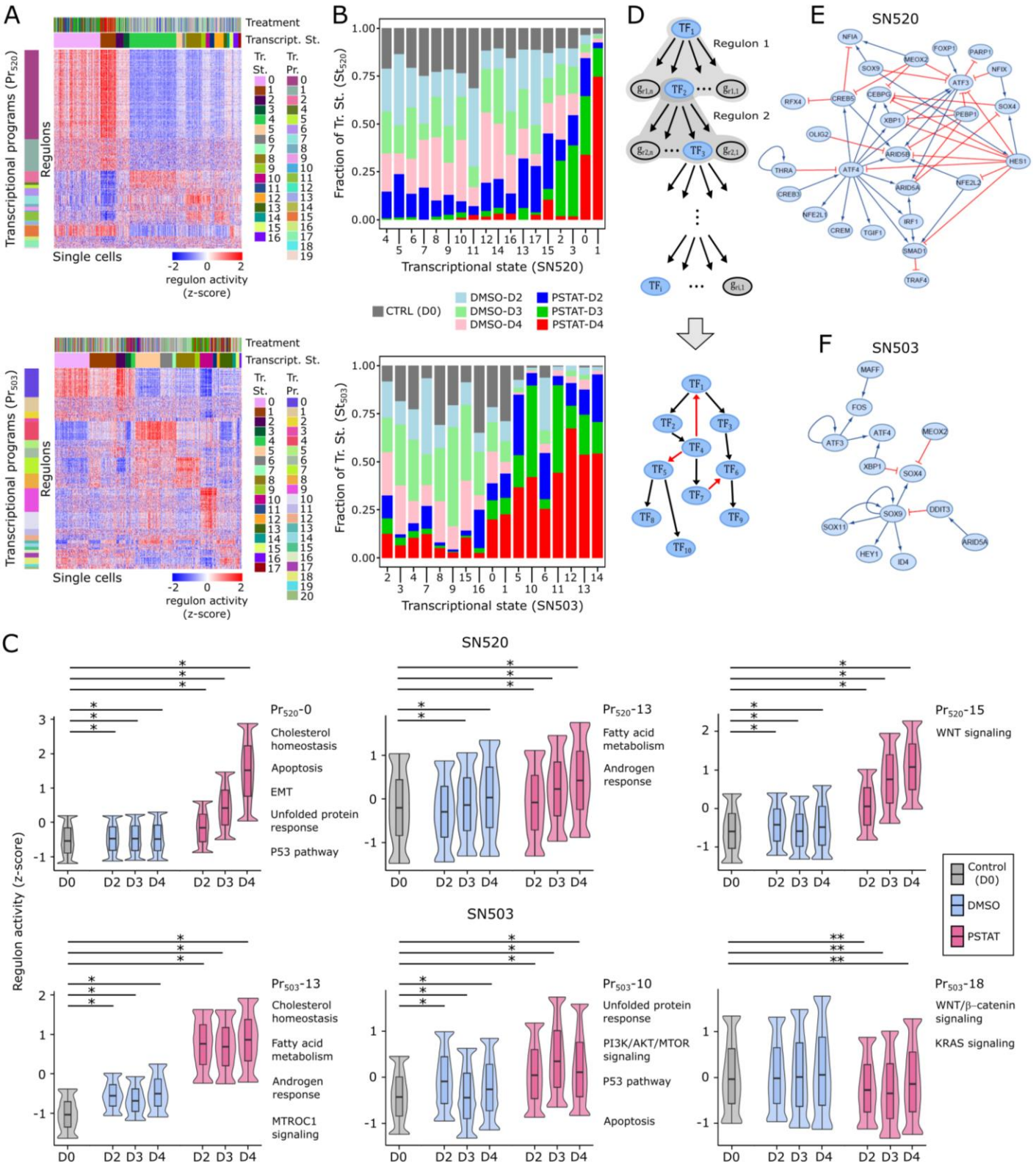

bioRxiv preprint doi: https://doi.org/10.1101/2024.02.02.578510; this version posted February 7, 2024. The copyright holder for this preprint (which was not certified by peer review) is the author/funder, who has granted bioRxiv a license to display the preprint in perpetuity. It is made available under aCC-BY-NC-ND 4.0 International license.

Figure 5

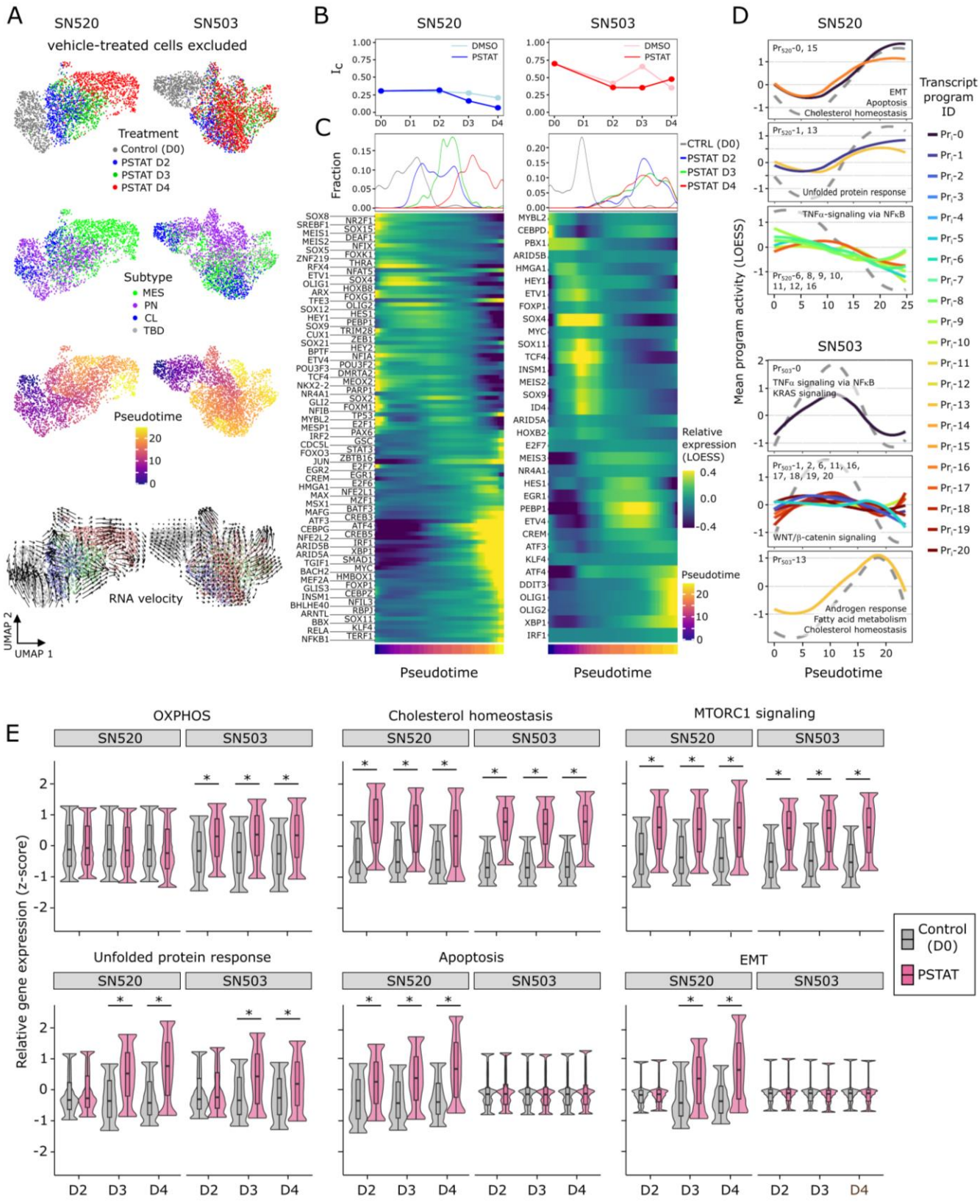

bioRxiv preprint doi: https://doi.org/10.1101/2024.02.02.578510; this version posted February 7, 2024. The copyright holder for this preprint (which was not certified by peer review) is the author/funder, who has granted bioRxiv a license to display the preprint in perpetuity. It is made available under aCC-BY-NC-ND 4.0 International license.

Figure 6

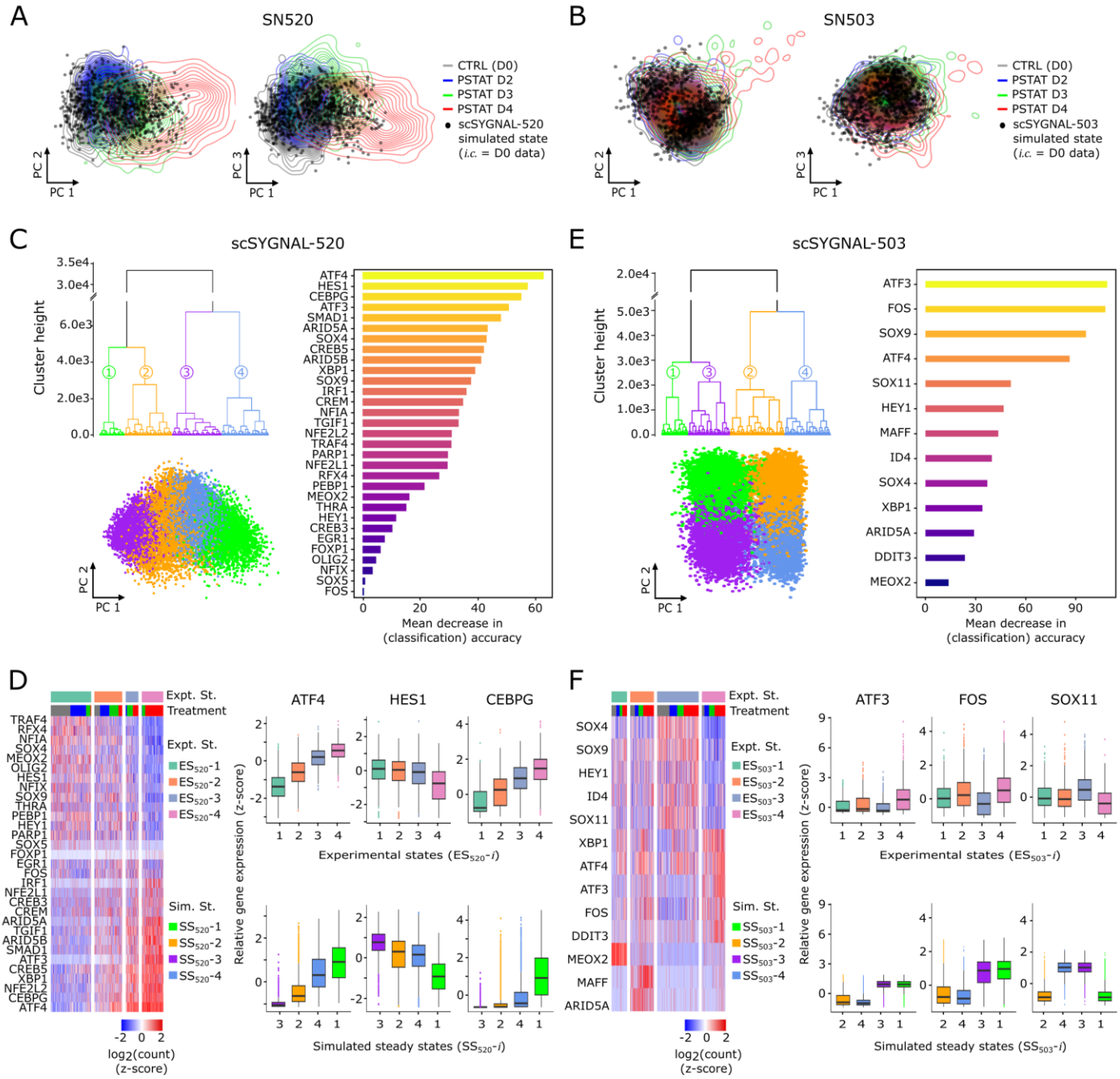

bioRxiv preprint doi: https://doi.org/10.1101/2024.02.02.578510; this version posted February 7, 2024. The copyright holder for this preprint (which was not certified by peer review) is the author/funder, who has granted bioRxiv a license to display the preprint in perpetuity. It is made available under aCC-BY-NC-ND 4.0 International license.

FIGURE 7

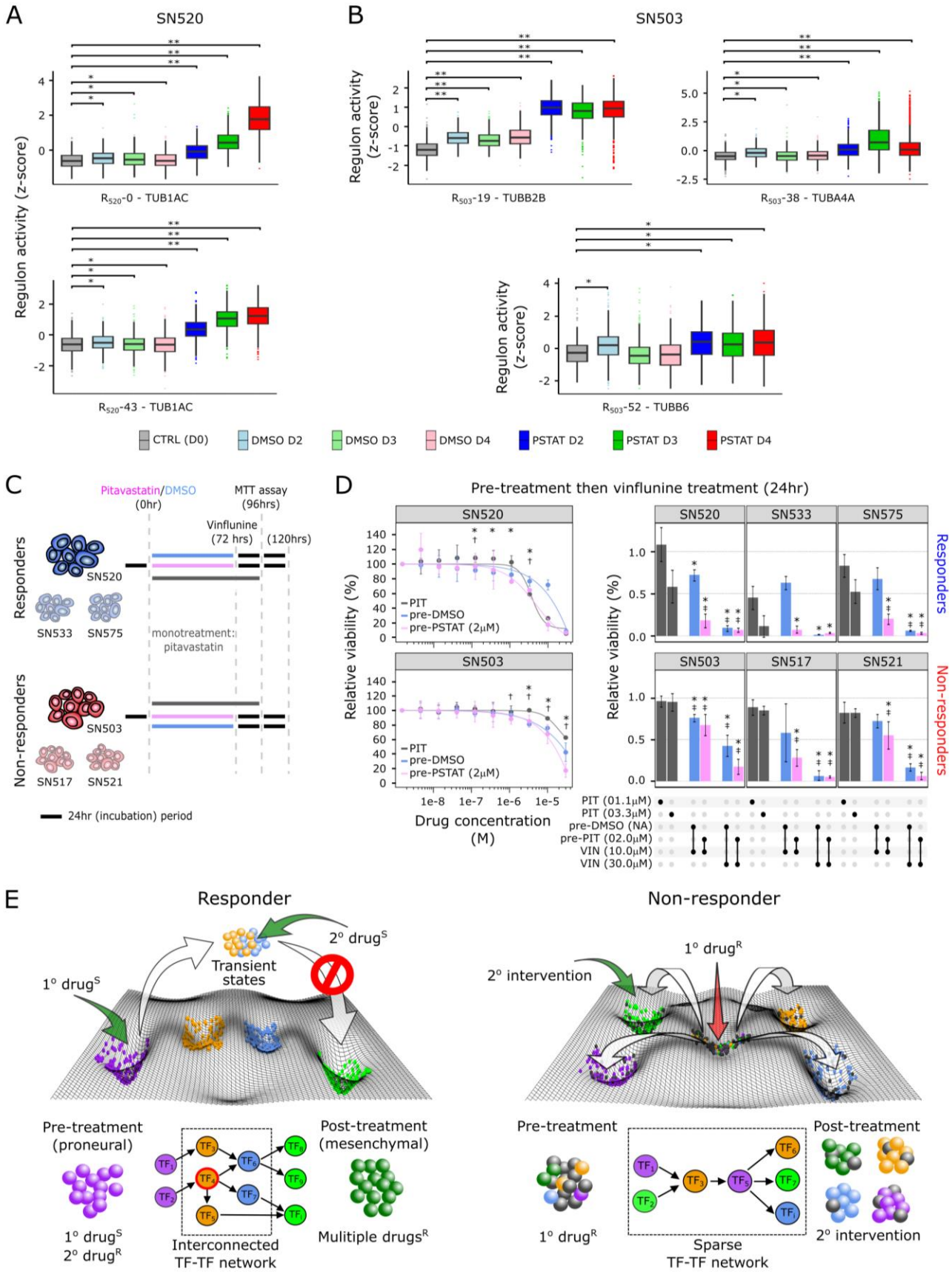

825